



The GOODS-N Jansky VLA 10 GHz Pilot Survey: Sizes of Star-forming μ JY Radio Sources

Eric J. Murphy^{1,2}, Emmanuel Momjian³, James J. Condon¹, Ranga-Ram Chary², Mark Dickinson⁴,
Hanae Inami⁴, Andrew R. Taylor^{5,6}, and Benjamin J. Weiner⁷

¹National Radio Astronomy Observatory, 520 Edgemont Road, Charlottesville, VA 22903, USA; emurphy@nrao.edu

²Infrared Processing and Analysis Center, California Institute of Technology, MC 314-6, Pasadena, CA 91125, USA

³National Radio Astronomy Observatory, P.O. Box O, 1003 Lopezville Road, Socorro, NM 87801, USA

⁴National Optical Astronomy Observatories, 950 N Cherry Avenue, Tucson, AZ 85719, USA

⁵Department of Astronomy, University of Cape Town, Rondebosch 7005, Republic of South Africa

⁶Department of Physics, University of the Western Cape, Belleville 7535, Republic of South Africa

⁷Steward Observatory, Department of Astronomy, University of Arizona, AZ 85721, USA

Received 2016 August 29; revised 2017 February 21; accepted 2017 February 22; published 2017 April 11

Abstract

Our sensitive ($\sigma_n \approx 572$ nJy beam⁻¹), high-resolution (FWHM $\theta_{1/2} = 0''.22 \approx 2$ kpc at $z \gtrsim 1$), 10 GHz image covering a single Karl G. Jansky Very Large Array (VLA) primary beam (FWHM $\Theta_{1/2} \approx 4''.25$) in the GOODS-N field contains 32 sources with $S_p \gtrsim 2$ μ Jy beam⁻¹ and optical and/or near-infrared (OIR) counterparts. Most are about as large as the star-forming regions that power them. Their median FWHM major axis is $\langle \theta_M \rangle = 167 \pm 32$ mas $\approx 1.2 \pm 0.28$ kpc, with rms scatter ≈ 91 mas ≈ 0.79 kpc. In units of the effective radius r_e that encloses half their flux, these radio sizes are $\langle r_e \rangle \approx 69 \pm 13$ mas $\approx 509 \pm 114$ pc, with rms scatter ≈ 38 mas ≈ 324 pc. These sizes are smaller than those measured at lower radio frequencies, but agree with dust emission sizes measured at mm/sub-mm wavelengths and extinction-corrected H α sizes. We made a low-resolution ($\theta_{1/2} = 1''.0$) image with $\approx 10\times$ better brightness sensitivity, in order to detect extended sources and measure matched-resolution spectral indices $\alpha_{1.4\text{ GHz}}^{10\text{ GHz}}$. It contains six new sources with $S_p \gtrsim 3.9$ μ Jy beam⁻¹ and OIR counterparts. The median redshift of all 38 sources is $\langle z \rangle = 1.24 \pm 0.15$. The 19 sources with 1.4 GHz counterparts have a median spectral index of $\langle \alpha_{1.4\text{ GHz}}^{10\text{ GHz}} \rangle = -0.74 \pm 0.10$, with rms scatter ≈ 0.35 . Including upper limits on α for sources not detected at 1.4 GHz flattens the median to $\langle \alpha_{1.4\text{ GHz}}^{10\text{ GHz}} \rangle \gtrsim -0.61$, suggesting that the μ Jy radio sources at higher redshifts—and hence those selected at higher rest-frame frequencies—may have flatter spectra. If the non-thermal spectral index is $\alpha_{\text{NT}} \approx -0.85$, the median thermal fraction of sources selected at median rest-frame frequency ≈ 20 GHz is $\gtrsim 48\%$.

Key words: galaxies: evolution – galaxies: fundamental parameters – galaxies: high-redshift – galaxies: star formation – radio continuum: general

1. Introduction

Most radio surveys aimed at measuring the star formation history of the universe have been made at 1.4 or 3 GHz (e.g., Schinnerer et al. 2007; Morrison et al. 2010; Smolčić et al. 2017, in press), so they are more sensitive to steep-spectrum synchrotron radiation than flat-spectrum free-free emission. Low frequencies have been favored because telescope primary beam areas decrease with frequency ($\Omega_{\text{PB}} \propto \nu^{-2}$) and the steep decimetric spectra of star-forming galaxies ($\langle \alpha \rangle \approx -0.7$, where $S_\nu \propto \nu^\alpha$ (Condon 1992)). This often causes “survey speed” to decline sharply with frequency $SS \propto \nu^{-3.4}$, if system temperature, bandwidth, etc. are fixed. For a detailed quantitative discussion, see Condon (2015). Although more difficult to detect, higher-frequency radio emission from galaxies provides independent information on galaxy energetics and the star-formation process. Constructing the star-formation history of the universe requires converting the synchrotron luminosities measured by low-frequency surveys to star formation rates via the tight, but empirical and local, far-infrared/radio correlation (de Jong et al. 1985; Helou et al. 1985; Yun et al. 2001). Surveys at observing frequencies $\gtrsim 10$ GHz measure flux densities closer to the rest-frame frequencies $\nu \gtrsim 30$ GHz, where the total radio emission is dominated by the free-free radiation that is more directly proportional to the rate of

massive star formation (e.g., Mezger & Henderson 1967; Turner & Ho 1983, 1985; Klein & Graeve 1986; Kobulnicky & Johnson 1999; Murphy et al. 2012a, 2015b; Nikolic & Bolton 2012), are still unbiased by dust emission or absorption, and yield higher angular resolution for a given array size.

Using the original VLA, Richards et al. (1998, 1999) reached $\sigma_n = 8.5$ μ Jy beam⁻¹ at 8.5 GHz in the Hubble Deep Field-North (HDF-N, Williams et al. 1996). The significantly increased bandwidth of the upgraded VLA now allows more sensitive surveys within a reasonable amount of observing time. Furthermore, the VLA will remain the only radio interferometer able to conduct such high-frequency radio continuum surveys until the SKA1-MID, equipped with the Band-5a/b (5–9.25 GHz/9–16.7 GHz) receivers, comes online in approximately $\gtrsim 2025$ (e.g., Murphy et al. 2015a).

In this paper, we present initial results on a flux-limited sample of galaxies from pilot observations aimed at mapping the entire Great Observatories Origins Deep Survey-North (GOODS-N; Dickinson et al. 2003; Giavalisco et al. 2004) field at 10 GHz. The GOODS-N field at J2000 $\alpha = 12^{\text{h}}36^{\text{m}}55^{\text{s}}$, $\delta = +62^\circ 14' 15''$ covers ≈ 160 arcmin² centered on the HDF-N, and is unrivaled in terms of its ancillary data. These include extremely deep *Chandra*, *Hubble Space Telescope* (HST), *Spitzer*, and *Herschel* observations, deep *UBVR1JHK* ground-based imaging, ~ 3500 spectroscopic redshifts from 8–10 m telescopes, and some of the deepest

1.4 GHz observations ever made (Morrison et al. 2010). Our new VLA X-band (8–12 GHz; reference frequency 10 GHz) pilot image has $\approx 15\times$ better point-source sensitivity than the Richards et al. (1998) image. Its $\theta_{1/2} \approx 0''.22$ angular resolution is well-matched to the resolution of *HST*/ACS optical and *HST*/WFC3-IR (continuum + H α imaging) data from GOODS and the Cosmic Assembly Near-infrared Deep Extragalactic Legacy Survey (CANDELS; Grogin et al. 2011; Koekemoer et al. 2011), and delivers a physical resolution of $\lesssim 1.9$ kpc at *any* redshift. Finally, the radio data provide an extinction-free view of the morphologies of dusty starburst galaxies that dominate the cosmic star formation activity between $1 \lesssim z \lesssim 3$ (e.g., Murphy et al. 2011a; Magnelli et al. 2013). In this redshift range, 10 GHz observations sample $20 \lesssim \nu \lesssim 40$ GHz in the source frame, where galaxy emission is expected to be dominated by free-free radiation (e.g., Murphy 2009), and thus provide accurate star formation rates for comparison with other diagnostics available from the GOODS ancillary data (e.g., FUV continuum, H α , [O III]5007 Å).

In this paper, we highlight our findings on the typical 10 GHz source characteristics, based on these new, extremely deep VLA data. The paper is organized as follows. In Section 2, we describe the data as well as the analysis procedures used in the present study. In Section 3, we present our results and discuss their implications. Our main conclusions are then summarized in Section 4. All calculations are made assuming a Hubble constant $H_0 = 71 \text{ km s}^{-1} \text{ Mpc}^{-1}$ and a flat Λ CDM cosmology with $\Omega_M = 0.27$ and $\Omega_\Lambda = 0.73$.

2. Data and Analysis

In this section, we describe our observations and imaging procedure. We additionally provide a detailed description of our source-finding and optical/NIR (OIR) cross-matching procedure, which was used to create a highly reliable final sample of sources.

2.1. Observations

We observed a single pointing, centered on J2000 $\alpha = 12^{\text{h}}36^{\text{m}}51^{\text{s}}.26$, $\delta = +62^\circ 13'37''.4$, over the 8–12 GHz X-band frequency range with the A- and C-configurations, as part of the project VLA/14B-037. We chose this pointing center to maximize the overlap of known sources in GOODS-N detected at other frequencies, specifically the 31–39 GHz continuum detections from VLA project VLA/13A-398 (PI: Riechers) that searched for redshifted 115 GHz CO $J = 1 \rightarrow 0$. These continuum detection results (J. Hodge et al. 2017, in preparation) remain unpublished, and are thus not included in the present analysis. We utilized two pairs of the 3-bit samplers of the VLA, each with 2 GHz bandwidth and dual polarization (R and L). For each sampler pair, the Wideband Interferometric Digital ARchitecture correlator delivered 16 sub-bands, each 128 MHz wide, with 2 MHz spectral channels and full polarization products (RR, LL, RL, LR).

The on-source integration times in the A- and C-configurations were roughly 23 and 1.5 hr, respectively. The A-configuration observations were carried out over seven separate runs during 2015 June, and the C-configuration observations were made during a single run in 2014 December. The source 3C 286 was used as the flux density scale and bandpass calibrator, whereas J1302+5748 was used as the complex gain and telescope

pointing calibrator. Full polarization information was additionally obtained, using 3C 286 to calibrate the polarization position angle and J1407+2827 as a instrumental polarization (leakage) calibrator. However, the polarization results will be deferred to a future paper. To reduce these data, we used the Common Astronomy Software Applications (CASA; McMullin et al. 2007) package and followed standard calibration and editing procedures, including the utilization of the VLA calibration pipeline.

2.2. Imaging

The calibrated A- and C-configuration measurement sets were imaged together, using the task TCLEAN in CASA version 4.6. The inclusion of the C-configuration data helps to fill in the hole in the (u, v) -plane left by the A-configuration data alone that, if not accounted for, will reduce the integrated flux densities of extended sources. The mode of TCLEAN was set to multifrequency synthesis (MFS; Conway et al. 1990; Sault & Wieringa 1994). After significant experimentation, we chose to use Briggs weighting with ROBUST = 0.5, and set the parameter NTERMS = 2. Here, NTERMS is the number of Taylor terms to model the frequency dependence of the sky emission. The value of 2 allows the MFS cleaning procedure to fit sources with different spectral indices, in addition to the sources' intensities. The use of Briggs weighting is necessary to suppress the broad pedestal of the naturally weighted dirty beam of the VLA A configuration, and thus helps to suppress sidelobes. To deconvolve extended low-intensity emission, we took advantage of the multiscale clean option (Cornwell 2008; Rau & Cornwell 2011) in CASA, searching for structures with scales up to $\approx 16\times$ the FWHM of the synthesized beam (i.e., about $\approx 2\times$ larger than the FWHM of the synthesized beam in the C configuration). We additionally invoked the W-projection algorithm (Cornwell et al. 2005, 2008), using 16 W-planes to take the non-coplanar nature of the array into account.

To improve the quality of the dirty beam by both making its shape more nearly Gaussian and further suppressing sidelobe structure, we applied a taper for baselines longer than $\sim 10^6 \lambda$. This taper was found to produce the best combination of brightness-temperature and point-source sensitivity. The main lobe of the dirty beam was nearly a circular Gaussian (major and minor FWHMs $\theta_{\text{maj}} = 0''.223 \times \theta_{\text{min}} = 0''.206$); thus, for simplicity, we restored the final image with a circular Gaussian with FWHM $\theta_{1/2} = 0''.22$. The final high-resolution image used in this analysis is a $10'$ on a side square; within 5% of the primary beam response, it has an rms noise $\sigma_n \approx 572 \text{ nJy beam}^{-1} \approx 139 \text{ mK}$ at the image center. For a primary beam FWHM at 10 GHz of $\Theta_{1/2} \approx 4''.25$, the image is approximately $2.35 \times \Theta_{1/2}$ on a side. For sources with typical spectral indices $\alpha \approx -0.7$, the point-source sensitivity at the center of the 10 GHz image is $\approx 2\times$ more sensitive than that of the Morrison et al. (2010) 1.4 GHz image, which has $\theta_{1/2} = 1''.7$ resolution and rms noise $\sigma_n \sim 4 \mu\text{Jy beam}^{-1}$.

We additionally made (u, v) -tapered images, with $1''$ and $2''$ synthesized beams, to increase the brightness-temperature sensitivity of our observations and investigate if our high-resolution image missed significant numbers of extended sources. The tapered $1''$ and $2''$ images have rms noises $\sigma_n \approx 1.1 \mu\text{Jy beam}^{-1}$ and $\sigma_n \approx 1.5 \mu\text{Jy beam}^{-1}$, respectively—roughly $2\times$ and $3\times$ higher than our full-resolution image, respectively. However, the corresponding brightness temperature rms values of the $1''$ and $2''$ tapered images are

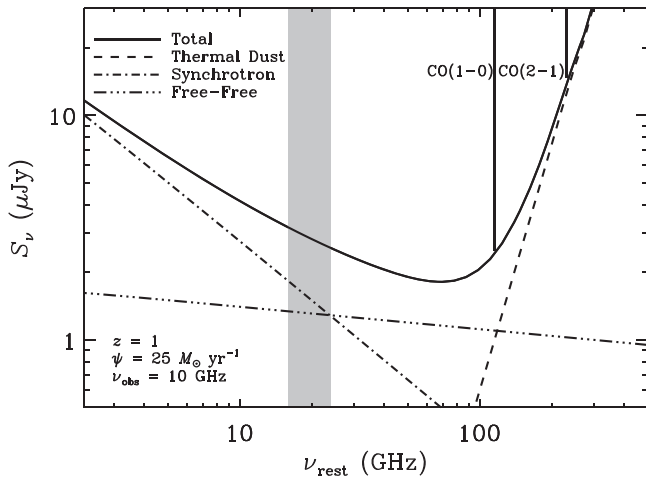


Figure 1. Model radio spectrum of a $z = 1$ galaxy, forming stars at a rate of $\psi \approx 25 M_{\odot} \text{ yr}^{-1}$. Synchrotron, free-free, and thermal dust emission components are identified, along with the $J = 2 \rightarrow 1$ and $J = 1 \rightarrow 0$ emission lines of CO. The grayed region identifies the rest-frame bandpass of our 10 GHz observations for such a source, illustrating that, at $z \gtrsim 1$, these data should become sensitive to free-free emission, and hence current star-formation activity in high-redshift galaxies.

$\sigma_n \approx 13 \text{ mK}$ and $\sigma_n \approx 4.7 \text{ mK}$, making them $\approx 10\times$ and $\approx 30\times$ lower than our full-resolution image, respectively.

2.2.1. Sensitivity of Deep Radio Imaging to Star-forming Galaxies at High Redshift

Coupling the relation between total infrared (IR; 8–1000 μm) luminosity and star-formation rate in Murphy et al. (2012b), Equation (15), which assumes a Kroupa (Kroupa 2001) initial mass function, with the locally measured IR-radio correlation (i.e., $q_{\text{IR}} = 2.64$; Bell 2003), the star-formation rate of a galaxy is related to its 1.4 GHz spectral luminosity by

$$\psi (M_{\odot} \text{ yr}^{-1}) \approx 5.16 \times 10^{-29} \left(\frac{L_{1.4 \text{ GHz}}}{\text{erg s}^{-1} \text{ Hz}^{-1}} \right). \quad (1)$$

At $z = 1$, a $5\sigma_n = 2.86 \mu\text{Jy beam}^{-1}$ 10 GHz point source with a spectral index $\alpha = -0.7$ has a spectral luminosity $L_{1.4 \text{ GHz}} \approx 4.85 \times 10^{29} \text{ erg s}^{-1} \text{ Hz}^{-1}$, so Equation (1) gives a star-formation rate of $\psi \approx 25 M_{\odot} \text{ yr}^{-1}$.

A model radio-to-far-infrared spectrum of such a galaxy is illustrated in Figure 1, indicating that these 10 GHz observations are highly sensitive to the amount of free-free emission at $z \gtrsim 1$, and hence current star formation. Furthermore, at the low radio flux densities achieved by our deep 10 GHz imaging, the fraction of active galactic nuclei (AGNs) detected relative to star-forming galaxies is extremely low (e.g., Condon 1984; Wilman et al. 2008). In Figure 4 of Wilman et al. (2008), the AGN fraction at several frequencies are shown including 1.4, 4.8, and 18 GHz, where the lowest AGN fraction ($\lesssim 10\%$) is found at the highest frequency of 18 GHz. Consequently, by being sensitive to free-free emission from galaxies forming stars at a rate of $\psi \gtrsim 25 M_{\odot} \text{ yr}^{-1}$ at $z \sim 1$, our 10 GHz data are sensitive to galaxies that contribute to roughly half of the cosmic star-formation rate density at these epochs (e.g., Murphy et al. 2011a; Magnelli et al. 2013). Furthermore, given this star-formation rate threshold, our data reach a mass-limit where the $z \sim 1$ cosmic star-formation rate density peaks, and hence down to the most representative star-forming sources at this epoch (Karim et al. 2011).

2.3. Source Finding and Photometry

We used the PYBDSM⁸ (Mohan & Rafferty 2015) source-detection package to locate and measure the integrated flux densities of the radio sources in each of our images. To do this, PYBDSM identifies “islands” of contiguous pixels above a detection threshold, and fits each island with Gaussians. We ran PYBDSM over the entire image using the standard default setting, except that we lowered the pixel threshold for keeping fitted sources from 5 to $3.5\sigma_n$. We adopted a minimum threshold of $3.5\sigma_n$, as we consider such sources that have optical identifications to be potentially significant. A primary beam correction was then applied to the reported peak brightnesses and integrated flux densities (along with their errors), using the frequency-dependent primary beam correction at 10 GHz, as given in EVLA Memo# 195 (Perley 2016).⁹ For this paper, we kept sources out to a radius of ≈ 3.9 from the phase center, where the sky response drops to $\approx 5\%$ of the on-axis value. For reference, the HWHM of the primary beam at 10 GHz is $\approx 2'.125$. A total of 1412 and 114 sources were “detected” (see Section 2.3.2) above a threshold of 3.5 and $5\sigma_n$, respectively. To assess the reliability of detections as faint as $3.5\sigma_n$, we used existing deep *HST* and *Spitzer* data to identify OIR counterparts.

In Table 1, we list the deconvolved source parameters from PYBDSM for detections from the full-resolution image that are confirmed by having OIR counterparts (see Section 2.3.1). Sources are split by their 10 GHz detection confidence, at a significance of either $S_P/\sigma_n \geq 5$ or $3.5 \leq S_P/\sigma_n < 5$. It is worth emphasizing that images from the full survey, which will include multiple pointings per source, will be able to confirm any questionable sources without OIR counterparts detected in these single-pointing pilot observations. Listed parameters include the source positions, peak brightnesses (S_P), integrated flux densities (S_I), best estimates for the total flux densities (S_*), and deconvolved FWHM source sizes ($\theta_M \times \theta_m$). Deconvolved source sizes were calculated such that

$$\theta = \sqrt{\phi^2 - \theta_{1/2}^2}, \quad (2)$$

where ϕ is the FWHM of the fitted major or minor axis. The uncertainties in the fitted parameters include the effects of correlated noise in synthesis images (Condon 1997). Uncertainties on the deconvolved source sizes were calculated from

$$\left(\frac{\sigma_{\theta}}{\sigma_{\phi}} \right) = \left[1 - \left(\frac{\theta_{1/2}}{\phi} \right)^2 \right]^{-1/2}. \quad (3)$$

For a few sources, PYBDSM fit multiple Gaussian components, typically including a very narrow component at the peak of the source. One instance of this is for the known FR I radio galaxy at $z = 1.013$ (Richards et al. 1998), where we are able to resolve some of its jet structure. Because we are interested in measuring the extent of star-forming galaxy disks, we used IMFIT in CASA to fit single Gaussians for these cases and report the corresponding deconvolved source parameters.

Individual sources are considered to be confidently resolved if $\phi_M - \theta_{1/2} \geq 2\sigma_{\phi_M}$; they are identified in Tables 1 and 2. For instances where PYBDSM reported unphysical fitted sizes, i.e.,

⁸ <http://www.astron.nl/citt/pybdsm/>

⁹ <https://library.nrao.edu/public/memos/evla/EVLAM-195.pdf>

Table 1
Full-Resolution 10 GHz Source Characteristics

R.A. (J2000)	Decl. (J2000)	z	z^a (type)	r^b (mas)	JH_{NIR}^c (mag)	S_{P} ($\mu\text{Jy beam}^{-1}$)	S_{I} (μJy)	S_* (μJy)	$\theta_{\text{M}} \times \theta_{\text{m}}$ (mas)
$S_{\text{P}}/\sigma_{\text{n}} \geq 5$									
12 36 34.211	+62 14 32.95	0.5184	1	31	19.52	7.72 ± 1.24	8.71 ± 2.09	8.20 ± 1.24	$148 \pm 86 \times 0 \pm 118$
^d 12 36 34.514	+62 12 41.08	1.2234	1	139	21.11	9.02 ± 1.23	27.90 ± 4.87	27.90 ± 4.87^e	$354 \pm 69 \times 283 \pm 59$
12 36 42.091	+62 13 31.43	2.018	1	16	23.76	37.81 ± 0.70	36.80 ± 1.22	37.30 ± 0.70	$42 \pm 23 \times 0 \pm 41$
12 36 42.214	+62 15 45.51	0.8575	1	173	20.02	27.78 ± 1.47	32.87 ± 2.42	32.87 ± 2.42^e	$144 \pm 28 \times 0 \pm 69$
12 36 44.110	+62 12 44.81	1.676	2	49	21.85	3.97 ± 0.74	4.46 ± 1.25	4.21 ± 0.74	$171 \pm 100 \times 0 \pm 120$
^d 12 36 44.386	+62 11 33.14	1.0128	1	30	19.46	279.25 ± 2.14	340.57 ± 4.25	340.57 ± 4.25^e	$139 \pm 4 \times 56 \pm 7$
12 36 46.063	+62 14 48.70	2.003	1	155	23.71	6.95 ± 0.82	10.65 ± 1.25	10.65 ± 1.25^e	$214 \pm 57 \times 101 \pm 62$
12 36 46.332	+62 14 04.69	0.9605	1	82	20.11	92.69 ± 0.64	91.06 ± 1.12	91.06 ± 1.12^e	$53 \pm 7 \times 0 \pm 25$
12 36 48.076	+62 13 09.01	0.4745	1	35	19.59	4.22 ± 0.64	4.38 ± 1.09	4.30 ± 0.64	$80 \pm 108 \times 0 \pm 121$
12 36 48.330	+62 14 16.57	2.002	1	149	22.55	3.20 ± 0.63	3.15 ± 1.13	3.17 ± 0.63	$146 \pm 114 \times 0 \pm 118$
12 36 52.884	+62 14 44.07	0.3208	1	18	18.22	114.69 ± 0.72	113.24 ± 1.25	113.96 ± 0.72	$25 \pm 13 \times 0 \pm 24$
12 36 53.367	+62 11 39.58	1.268	1	45	21.47	5.43 ± 1.03	20.82 ± 1.28	20.82 ± 1.28^e	$553 \pm 140 \times 220 \pm 73$
12 36 55.449	+62 13 11.24	0.9544	1	11	20.63	20.11 ± 0.64	20.53 ± 1.11	20.32 ± 0.64	$54 \pm 31 \times 0 \pm 55$
12 36 56.914	+62 13 01.64	1.2409	1	21	21.16	8.69 ± 0.66	8.12 ± 1.17	8.40 ± 0.66	$24 \pm 160 \times 0 \pm 82$
12 36 58.843	+62 14 34.92	0.6766	1	34	19.75	4.71 ± 0.77	4.86 ± 1.32	4.78 ± 0.77	$110 \pm 98 \times 0 \pm 119$
12 37 04.873	+62 16 01.55	1.170	1	16	23.20	12.83 ± 2.24	13.02 ± 3.93	12.92 ± 2.24	$145 \pm 99 \times 0 \pm 113$
12 37 11.251	+62 13 30.87	1.9958	1	11	22.40	7.48 ± 1.35	8.15 ± 2.34	7.81 ± 1.35	$181 \pm 100 \times 0 \pm 113$
12 37 11.984	+62 13 25.69	1.992	1	92	23.26	7.30 ± 1.41	7.03 ± 2.56	7.16 ± 1.41	$152 \pm 113 \times 0 \pm 113$
12 37 16.376	+62 15 12.35	0.5577	1	60	19.15	87.07 ± 4.03	95.58 ± 6.78	91.22 ± 4.03	$96 \pm 29 \times 23 \pm 94$
$3.5 \leq S_{\text{P}}/\sigma_{\text{n}} < 5$									
12 36 19.565	+62 13 42.93	1.699	3	159	25.43	31.16 ± 6.76	31.68 ± 11.85	31.42 ± 6.76	$141 \pm 124 \times 0 \pm 128$
12 36 27.872	+62 14 49.08	0.6802	1	50	19.96	12.78 ± 2.65	25.68 ± 3.78	18.12 ± 2.65	$318 \pm 112 \times 122 \pm 93$
12 36 35.592	+62 14 24.04	2.0150	1	64	21.45	4.90 ± 1.12	12.32 ± 1.51	7.77 ± 1.12	$377 \pm 131 \times 171 \pm 91$
12 36 40.306	+62 13 31.14	0.484	1	66	21.24	3.39 ± 0.72	3.88 ± 1.26	3.63 ± 0.72	$238 \pm 126 \times 0 \pm 112$
12 36 41.604	+62 13 49.41	3.244	3	62	24.37	3.20 ± 0.76	5.01 ± 1.16	4.00 ± 0.76	$246 \pm 121 \times 65 \pm 166$
12 36 42.128	+62 13 48.34	0.817	3	81	25.32	3.25 ± 0.71	3.41 ± 1.22	3.33 ± 0.71	$119 \pm 127 \times 0 \pm 138$
12 36 46.736	+62 14 45.84	2.004	1	93	22.47	3.45 ± 0.75	3.58 ± 1.29	3.51 ± 0.75	$87 \pm 148 \times 0 \pm 146$
12 36 48.524	+62 14 36.91	1.365	3	88	26.68	2.93 ± 0.69	2.95 ± 1.21	2.94 ± 0.69	$126 \pm 138 \times 0 \pm 138$
12 36 49.688	+62 13 13.01	0.4745	1	179	20.61	2.44 ± 0.66	3.32 ± 1.03	2.84 ± 0.66	$173 \pm 131 \times 85 \pm 164$
12 36 57.375	+62 14 07.86	1.460	1	73	22.03	2.95 ± 0.65	3.21 ± 1.14	3.07 ± 0.65	$199 \pm 125 \times 0 \pm 120$
12 36 59.614	+62 11 53.36	1.0205	1	55	21.76	4.25 ± 1.11	6.00 ± 1.75	5.05 ± 1.11	$237 \pm 137 \times 0 \pm 150$
12 37 02.539	+62 13 02.32	2.650	4	145	25.63	4.14 ± 0.83	6.84 ± 1.26	5.32 ± 0.83	$292 \pm 112 \times 0 \pm 131$
12 37 08.748	+62 12 57.83	2.268	1	107	23.12	5.89 ± 1.22	7.04 ± 2.01	6.44 ± 1.22	$162 \pm 107 \times 0 \pm 137$

Notes.

^a Redshift type: (1) Spectroscopic (Cohen et al. 2000; Swinbank et al. 2004; Wirth et al. 2004; Treu et al. 2005; Reddy et al. 2006; Barger et al. 2008; Frayer et al. 2008; Teplitz et al. 2011; D. Stern et al. 2017, in preparation; this paper); (2) Grism-based (Momcheva et al. 2016); (3) Photometric (Momcheva et al. 2016); (4) Photometric (G. Barro et al. 2017, in preparation; D. Kodra et al. 2017, in preparation).

^b The angular separation between the 10 GHz detection and the OIR counterpart.

^c NIR magnitude from some combination of J_{125} , JH_{140} and H_{160} *HST*/WFC3 images, scaled to the JH_{140} AB zeropoint as described in (Momcheva et al. 2016).

^d Single-Gaussian, fitted parameters reported by IMFIT because the PYBDSM fit included multiple Gaussian components.

^e Confidently ($\geq 2\sigma_{\phi}$) resolved.

equal to or smaller than the synthesized beam, a size of 0 is listed in Tables 1 and 2, where the associated uncertainty corresponds to the 1σ upper limit of the deconvolved source size. For sources whose major axes are resolved, the integrated flux densities from the source fitting are taken as the best estimate for the sources total flux density (S_*). For sources whose fitted major axes are less than $2\sigma_{\phi_{\text{M}}}$ larger than the synthesized beam, we instead take their total flux density to be the geometric mean of the peak brightness and integrated flux densities, as reported by PYBDSM (Condon 1997).

In Table 2, we similarly list the deconvolved source parameters and photometry from the $1''$ (u, v)-tapered image, or from the $2''$ image in the three cases where the total flux density in the $2''$ image is $>3\sigma$ larger than in the $1''$ image. The flux densities recovered in the $2''$ tapered image for these three

sources are larger by factors of $\approx 1.1, 2.9,$ and $1.2,$ in order of their appearance in Table 2.

2.3.1. Optical Identification

We identified our radio sources with their OIR counterparts in Momcheva et al. (2016) by position coincidence, using the criteria presented in the appendix of Condon et al. (1975). The radio position accuracy is noise-limited, so the one-dimensional radio position errors parallel to the fitted FWHM major axis ϕ_{M} and minor axis ϕ_{m} are Gaussian distributed, with rms

$$\sigma_{\text{M}} \approx \frac{\phi_{\text{M}}}{\sqrt{8 \ln 2}} \left(\frac{\sigma_{\text{P}}}{S_{\text{P}}} \right) \quad \text{and} \quad \sigma_{\text{m}} \approx \frac{\phi_{\text{m}}}{\sqrt{8 \ln 2}} \left(\frac{\sigma_{\text{P}}}{S_{\text{P}}} \right), \quad (4)$$

Table 2
1'' Tapered 10 GHz Source Characteristics

R.A. (J2000)	Decl. (J2000)	z	z^a (type)	r^b	JH_{NIR}^c (mag)	S_{P} ($\mu\text{Jy beam}^{-1}$)	S_{I} (μJy)	S_{*} (μJy)	$\theta_{\text{M}} \times \theta_{\text{m}}$	$\alpha_{1.4\text{ GHz}}^{10\text{ GHz}}$	$f_{\text{T}}^{i,d}$
$S_{\text{P}}/\sigma_n \geq 5$											
^c 12 36 34.460	+62 12 12.93	0.4573	1	0''16	18.12	22.66 \pm 2.97	49.58 \pm 4.13	49.58 \pm 4.13 ^f	1''37 \pm 0''30 \times 0''82 \pm 0''25	-0.77 \pm 0.05	0.19 \pm 0.11
12 36 34.502	+62 12 41.04	1.2234	1	0''19	21.11	27.03 \pm 2.42	36.71 \pm 3.80	31.50 \pm 2.42	0''68 \pm 0''20 \times 0''51 \pm 0''21	-0.94 \pm 0.05	0.21 \pm 0.09
12 36 35.594	+62 14 24.16	2.011	1	0''18	21.45	12.07 \pm 2.12	18.16 \pm 3.27	14.80 \pm 2.12	1''03 \pm 0''40 \times 0''32 \pm 0''53	-0.83 \pm 0.09	0.04 \pm 0.22
12 36 42.084	+62 13 31.41	2.018	1	0''03	23.76	52.37 \pm 1.37	67.01 \pm 2.20	67.01 \pm 2.20 ^f	0''65 \pm 0''06 \times 0''39 \pm 0''07	-1.02 \pm 0.02	0.21 \pm 0.04
12 36 42.215	+62 15 45.50	0.8575	1	0''18	20.02	36.34 \pm 2.77	41.84 \pm 4.60	38.99 \pm 2.77	0''58 \pm 0''19 \times 0''00 \pm 0''38	-0.69 \pm 0.05	0.35 \pm 0.09
^e 12 36 44.385	+62 11 33.13	1.0128	1	0''04	19.46	426.08 \pm 3.42	449.83 \pm 5.83	449.83 \pm 5.83 ^f	0''69 \pm 0''05 \times 0''00 \pm 0''25	-0.71 \pm 0.02	0.32 \pm 0.03
^g 12 36 46.052	+62 14 48.73	2.003	1	0''16	23.71	13.33 \pm 2.19	35.13 \pm 2.90	35.13 \pm 2.90 ^f	2''75 \pm 0''71 \times 2''36 \pm 0''65	-0.58 \pm 0.05	0.54 \pm 0.07
^g 12 36 46.332	+62 14 04.70	0.9605	1	0''08	20.11	125.72 \pm 1.74	138.89 \pm 2.91	138.89 \pm 2.91 ^f	0''75 \pm 0''09 \times 0''53 \pm 0''11	-0.43 \pm 0.02	0.73 \pm 0.02
12 36 49.692	+62 13 13.03	0.4745	1	0''15	20.61	6.61 \pm 1.20	13.30 \pm 1.71	13.30 \pm 1.71 ^f	1''46 \pm 0''45 \times 0''54 \pm 0''37	-0.76 \pm 0.10	0.21 \pm 0.21
^h 12 36 52.876	+62 14 44.06	0.3208	1	0''05	18.22	137.92 \pm 1.59	191.51 \pm 3.46	191.51 \pm 3.46 ^f	0''66 \pm 0''03 \times 0''59 \pm 0''03	-0.02 \pm 0.03	1.00 \pm 0.01
12 36 53.361	+62 11 39.57	1.268	1	0''05	21.47	16.00 \pm 2.07	19.02 \pm 3.41	17.45 \pm 2.07	0''61 \pm 0''31 \times 0''16 \pm 0''77	-0.80 \pm 0.08	0.12 \pm 0.19
12 36 55.448	+62 13 11.21	0.9544	1	0''02	20.63	18.30 \pm 1.13	15.93 \pm 2.05	17.07 \pm 1.13	0''00 \pm 0''36 \times 0''00 \pm 0''33	\geq -0.07	\geq 1.00
12 36 56.919	+62 13 01.76	1.2409	1	0''10	21.16	8.52 \pm 1.28	13.93 \pm 1.95	13.93 \pm 1.95 ^f	1''29 \pm 0''37 \times 0''07 \pm 1''76	\geq -0.17	\geq 0.96
12 37 16.372	+62 15 12.32	0.5577	1	0''03	19.15	113.95 \pm 7.81	132.98 \pm 12.92	132.98 \pm 12.92 ^f	0''64 \pm 0''16 \times 0''00 \pm 0''36	-0.05 \pm 0.06	1.00 \pm 0.03
$3.5 \leq S_{\text{P}}/\sigma_n < 5$											
12 36 27.861	+62 14 49.07	0.6802	1	0''13	19.96	18.92 \pm 4.73	18.72 \pm 8.40	18.82 \pm 4.73	0''64 \pm 0''66 \times 0''00 \pm 0''62	\geq -0.02	\geq 1.00
12 36 34.227	+62 14 33.09	0.5184	1	0''18	19.52	9.14 \pm 2.19	8.40 \pm 4.04	8.77 \pm 2.19	0''64 \pm 0''66 \times 0''00 \pm 0''56	-0.54 \pm 0.15	0.59 \pm 0.21
^c 12 36 43.963	+62 12 50.08	0.557	1	0''07	20.13	5.01 \pm 1.35	8.04 \pm 2.09	6.35 \pm 1.35	1''43 \pm 0''73 \times 0''00 \pm 0''65	-0.89 \pm 0.16	0.22 \pm 0.31
^c 12 36 44.010	+62 14 50.77	1.784	1	0''23	22.62	6.25 \pm 1.60	9.33 \pm 2.48	7.63 \pm 1.60	1''10 \pm 0''60 \times 0''09 \pm 2''57	-0.74 \pm 0.16	0.26 \pm 0.32
12 36 44.101	+62 12 44.58	1.676	2	0''26	21.85	5.79 \pm 1.39	8.13 \pm 2.22	6.86 \pm 1.39	1''16 \pm 0''60 \times 0''00 \pm 0''62	\geq -0.53	\geq 0.60
^c 12 36 46.377	+62 16 29.56	0.5032	1	0''33	19.36	22.99 \pm 4.81	29.50 \pm 7.71	26.04 \pm 4.81	0''70 \pm 0''48 \times 0''33 \pm 0''66	-1.43 \pm 0.10	0.19 \pm 0.16
12 36 48.292	+62 14 16.59	2.002	1	0''10	22.55	4.55 \pm 1.26	6.32 \pm 1.98	5.37 \pm 1.26	0''81 \pm 0''61 \times 0''40 \pm 0''75	\geq -0.66	\geq 0.41
^c 12 36 50.104	+62 14 01.08	2.231	1	0''07	23.65	5.57 \pm 1.20	7.54 \pm 1.89	6.48 \pm 1.20	0''62 \pm 0''49 \times 0''57 \pm 0''50	\geq -0.56	\geq 0.56
^c 12 36 55.026	+62 12 52.22	0.9929	3	0''12	25.09	4.71 \pm 1.30	7.26 \pm 1.99	5.85 \pm 1.30	1''04 \pm 0''62 \times 0''37 \pm 0''75	\geq -0.61	\geq 0.48
12 36 58.844	+62 14 34.97	0.6766	1	0''09	19.75	6.43 \pm 1.47	8.08 \pm 2.38	7.21 \pm 1.47	0''76 \pm 0''53 \times 0''00 \pm 0''67	\geq -0.51	\geq 0.64
12 37 02.547	+62 13 02.18	2.650	4	0''17	25.63	5.89 \pm 1.53	13.52 \pm 2.13	8.92 \pm 1.53	1''82 \pm 0''75 \times 0''48 \pm 0''55	-0.54 \pm 0.12	0.60 \pm 0.17
12 37 04.894	+62 16 01.46	1.170	1	0''18	23.20	19.30 \pm 4.39	19.92 \pm 7.52	19.61 \pm 4.39	0''27 \pm 0''93 \times 0''00 \pm 0''70	-0.19 \pm 0.14	0.94 \pm 0.10
12 37 11.321	+62 13 30.86	1.9958	1	0''22	21.70	11.70 \pm 2.63	22.64 \pm 3.86	16.28 \pm 2.63	1''67 \pm 0''64 \times 0''00 \pm 0''62	-1.06 \pm 0.09	0.20 \pm 0.17

Notes.

^a Redshift type: (1) Spectroscopic (Cohen et al. 2000; Swinbank et al. 2004; Wirth et al. 2004; Treu et al. 2005; Reddy et al. 2006; Barger et al. 2008; Frayer et al. 2008; Teplitz et al. 2011; D. Stern et al. 2017, in preparation; this paper); (2) Grism-based (Momcheva et al. 2016); (3) Photometric (Momcheva et al. 2016); (4) Photometric (G. Barro et al. 2017, in preparation; D. Kodra et al. 2017, in preparation).

^b The angular separation between the 10 GHz detection and the OIR counterpart.

^c NIR magnitude from some combination of J_{125} , JH_{140} and H_{160} *HST*/WFC3 images, scaled to the JH_{140} AB zeropoint as described in (Momcheva et al. 2016).

^d Thermal fraction at the rest-frame frequency ($\nu_{\text{r}}/\text{GHz}$) = $10(1+z)$.

^e Not detected in the full-resolution image.

^f Confidently ($\geq 2\sigma_{\theta}$) resolved.

^g 2'' tapered image used in photometry because significantly (i.e., $>3\sigma$) more flux is recovered.

^h Single-Gaussian, fitted parameters reported by IMFIT because the PYBDSM fit included multiple Gaussian components.

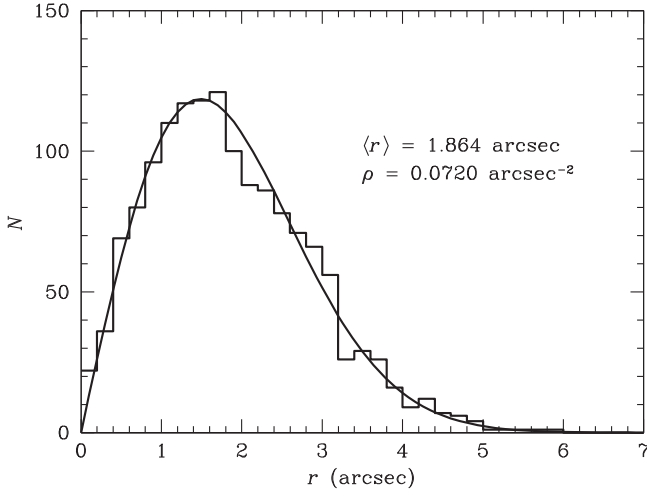


Figure 2. Histogram showing the offsets r of OIR candidates from 1454 random positions in the radio image is well-matched by the Rayleigh distribution expected for an OIR sky density $\rho = 0.0720 \text{ arcsec}^{-2}$.

respectively, where $(S_p/\sigma_p \approx S_p/\sigma_n)$ is the fitted peak signal-to-noise ratio (S/N). Even $S/N = 5$ point sources have very small $\sigma_M \approx \sigma_m \approx 0''.019$. Nearly all of the OIR identifications have very high S/N, so their rms uncertainties σ_{OIR} are dominated by systematic differences between the OIR and radio reference frames. We made preliminary identifications, and found systematic OIR minus radio offsets $\Delta\alpha = +3 \text{ mas}$ and $\Delta\delta = +30 \text{ mas}$. After these offsets were removed, the remaining OIR errors have zero mean and rms $\sigma_{\text{OIR}} \approx 0''.025$.

If the radio and OIR sources coincide exactly on the sky, their measured radio-optical offsets r should have a Rayleigh distribution

$$P(r) = \frac{r}{\sigma^2} \exp\left(-\frac{r^2}{2\sigma^2}\right), \quad (5)$$

with

$$\sigma \approx \sqrt{\left(\frac{\phi_M}{\sqrt{8 \ln 2}} \frac{\sigma_n}{S_p}\right)^2 + \sigma_{\text{OIR}}^2}. \quad (6)$$

The probability distribution of the angular distance r from a radio source to the nearest unrelated optical object is

$$P(r) = 2\pi\rho r \exp(-\pi\rho r^2), \quad (7)$$

where ρ is the sky density of optical identification candidates. The mean angular distance to the nearest unrelated optical object is

$$\langle r \rangle = \frac{1}{2\sqrt{\rho}}. \quad (8)$$

Figure 2 shows the distribution of angular distances r to the OIR sources nearest to a large sample of random positions in our fields (histogram) and the best-fit Rayleigh distribution, which implies $\rho \approx 0.0720 \text{ arcsec}^{-2}$.

To avoid incorrect optical identifications, it is necessary to keep $\rho\sigma^2 \ll 1$. The quantity $k \equiv (1 + 2\pi\rho\sigma^2)$ measures the identification candidate sky density in units of σ^2 , and $m \equiv r_s/\sigma$ describes the search radius r_s in units of the rms position error. For $\rho \approx 0.0720 \text{ arcsec}^{-2}$ and $\sigma \approx 0''.03$, $k \approx 1.00041$.

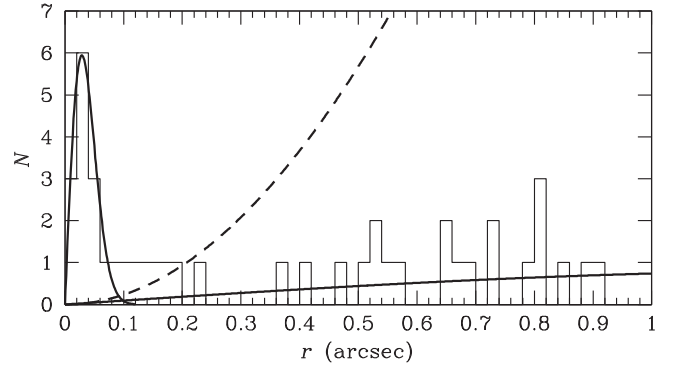


Figure 3. Histogram showing the number N of radio sources per bin of width $\Delta r = 0''.02$ with nearest OIR neighbors at angular offsets $r < 1''$. The sharp Rayleigh distribution matches the observed 14 sources identified by position coincidence with $m < 3$ and median $\langle \sigma \rangle \approx 0''.03$. The broad curve is the expected differential distribution for unrelated OIR objects with sky density $\rho = 0.0720 \text{ arcsec}^{-2}$, and the dashed curve is the calculated cumulative distribution $N(>r)$. It predicts one unrelated optical object will fall within $r = 0''.2$ of a $5\sigma_n$ radio source.

The final quantity needed to calculate the completeness C and reliability R of position-coincidence identifications is the fraction f of sources that have OIR counterparts brighter than some magnitude cutoff. The resulting identifications should have completeness

$$C = \frac{1 - \exp(-m^2k/2)}{k} \quad (9)$$

and reliability

$$R = C \left[\frac{1}{f} + \left(1 - \frac{1}{f}\right) \exp[m^2(1 - k)/2] - \exp(-m^2k/2) \right]^{-1}. \quad (10)$$

The best choice of the free parameter m limiting the search radius is a compromise between high completeness (large m ensures that true associations are not overlooked) and high reliability (low m avoids incorrect identifications with unrelated OIR objects nearby on the sky); it usually lies in the range $2 < m < 3$. The value of k in our sample is so small that we can safely choose $m = 3$. This ensures high completeness $C \approx 0.989$, and high reliability $R > 0.983$ for any value of $f > 0.1$.

The histogram in Figure 3 shows the distribution of radio/OIR offsets $r < 1''$ for all 114 radio sources with $S/N \geq 5$ in our high-resolution ($0''.22$) image. The sharp Rayleigh distribution cut-off near $r = 0''.09$ fits the $N = 14$ identifications with $m < 3$ and $\langle \sigma \rangle \approx 0''.03$. The slowly rising solid curve indicates the number of unrelated OIR objects with sky density $\rho = 0.0720(114 - 14)/114 \text{ arcsec}^{-2}$ expected per bin of width $\Delta r = 0''.02$, and the dashed curve is their calculated cumulative distribution $N(>r)$. The observed density of unrelated OIR objects matches the calculated curves quite well for $0''.2 < r < 1''$, indicating that clustering on scales $\lesssim 1''$ (i.e., $\lesssim 8 \text{ kpc}$ at $z \gtrsim 1$) does not detectably increase the number of nearby OIR objects. However, there are five “unexpected” OIR objects with $0''.09 \lesssim r \lesssim 0''.2$ where we expected only one in our sample of 114 radio sources. This

discrepancy reveals that the OIR identifications of some faint radio sources may actually be slightly offset in position; in particular, the most intense radio emission may come from a dusty star-forming region in a merging system with patchy OIR obscuration. For example, an $r \approx 0''.6$ (4 kpc) separation was measured between rest-frame UV and far-infrared emission peaks in the high-redshift starburst galaxy GN20 (Hodge et al. 2015). We inspected the OIR images of the five “unexpected” objects, and estimate that four of the five sources in Table 1 with $S_P/\sigma_n \geq 5$ and $0''.09 < r < 0''.2$ are correctly identified.

We carried out a similar analysis to assess the reliability of sources between $3.5 \leq S_P/\sigma_n < 5$, for which there was a total of 544 sources in the relative gain-weighted beam solid angle. For an $S/N = 3.5$, Equation (6) gives an rms position error of $\sigma = 0''.37$. Setting $m = 3$, we estimate a total of 1.5 false detections within a search radius of $r < 0''.11$. In Table 1, there are three $3.5 \leq S_P/\sigma_n < 5$ sources with $0''.11 < r < 0''.2$ that we consider to be reliable because one is associated with a bright $JH_{\text{NIR}} = 20.61$ mag galaxy, another is additionally detected at 1.4 GHz, and the third is associated with a heavily obscured, morphologically disturbed galaxy, for which a large offset appears physical based on a visual inspection.

We report a total of 32 reliable identifications for radio sources detected at $\geq 3.5\sigma_n$ significance in our full-resolution 10 GHz image. The median positional uncertainty among these 32 sources is $\langle 3\sigma \rangle \approx 0''.1$, which is typically larger than the median measured separation between the OIR and radio positions $\langle r \rangle \approx 64 \pm 11$ mas. However, there are nine instances ($\approx 30\%$) where the radio and OIR separation exceeds 3σ by a median of $\approx 53 \pm 12$ mas $\lesssim 0.41 \pm 0.10$ kpc at any redshift. The median distance between the radio and OIR centroids for the nine offset identifications is 149 ± 13 mas $\lesssim 1.17 \pm 0.10$ kpc.

In the $1''$ resolution image, we report a total of 27 reliable identifications detected at $\geq 3.5\sigma$ and matched to an OIR counterpart, six of which are not detected in the full-resolution image. The median positional uncertainty among these 27 sources is $\langle 3\sigma \rangle \approx 0''.3$, which is typically larger than the measured separation between the OIR and radio positions, with a median separation of $\approx 126 \pm 19$ mas. In this image, the radio and OIR separation for four sources is found to be larger than the 3σ positional uncertainty by a median value of $\approx 31 \pm 13$ mas, or $\approx 262 \pm 102$ pc at their distances. In other terms, the median distance between the radio and OIR centroids for these four sources is 188 ± 66 mas, or $\lesssim 1.6 \pm 0.4$ kpc at any redshift.

In Tables 1 and 2, spectroscopic redshifts (Cohen et al. 2000; Swinbank et al. 2004; Wirth et al. 2004; Treu et al. 2005; Reddy et al. 2006; Barger et al. 2008; Frayer et al. 2008; Teplitz et al. 2011; D. Stern et al. 2017, in preparation; this paper) are given, along with grism and photometric redshifts included in Momcheva et al. (2016). Additional notes on specific redshifts can be found in Appendix A. In every case, we provide the angular separation r between the 10 GHz detection and the OIR counterpart plus the NIR magnitude (JH_{NIR}) that is derived from some combination of J_{125} , JH_{140} , and H_{160} *HST*/WFC3 images, scaled to the JH_{140} AB zeropoint as described in Momcheva et al. (2016). We present image cutouts for three examples of 10 GHz sources matched to *HST* counterparts in Figure 4, one of which illustrates how dust obscuration can cause a statistically significant offset between the radio and OIR positions.

2.3.2. A Warning about $5\sigma_n$ “Detections” in Sparse Images

There are 114 sources with $S/N \geq 5$ in our image, which covers $\Omega = 3.6 \times 10^5$ arcsec² with $\theta_{1/2} = 0''.22$ FWHM resolution. The noise has the same angular power spectrum as the synthesized beam, so there are $N_n \approx 8 \ln(2)\Omega/(\pi\theta_{1/2}^2) \approx 1.3 \times 10^7$ independent noise samples in our image. The image noise amplitude distribution (Figure 5) is nearly, but not perfectly, Gaussian. If it were perfectly Gaussian, the probability that any sample would exceed $+5\sigma_n$ is only $P(>+5\sigma_n) = 2.87 \times 10^{-7}$, and there would be only $N_n P(>+5\sigma_n) \sim 4$ false radio sources stronger than $+5\sigma_n$. However, we believe that nearly all of the 95 optically unidentified $5\sigma_n$ sources are actually spurious for several reasons: (1) The histogram of the S/Ns for the 95 unidentified sources is extremely steep and cuts off below $S/N = 6.2$. (2) We cannot match any of these 95 sources reliably to sources in the extremely deep *Spitzer*/IRAC data at 3.6 or 4.5 μm , within a $1''$ radius, using catalogs compiled from Elbaz et al. (2011), which would be surprising if these sources existed, even within heavily obscured galaxies. (3) The 95 unidentified sources are uniformly distributed across the primary beam, as one would expect for random noise; they are not concentrated toward the center of the primary beam where real sources are stronger. (4) We found a similar number (92) of sources more negative than $-5\sigma_n$ in our high-resolution image by multiplying the image intensity units by -1 and running PyBDSM to find negative sources.

We believe that the false $\pm 5\sigma$ “detections” in our high-resolution image are simply the result of faint non-Gaussian image fluctuations related to unedited RFI, imperfectly cleaned sidelobes, and calibration errors. The lesson here is that sources in very sparse images (many clean beam solid angles per source) cannot be trusted at the $5\sigma_n$ level, even if the image noise looks perfectly uniform and Gaussian to the human eye.

Low-resolution images covering fewer beam solid angles, or low-frequency images containing larger numbers of sources, should yield more reliable $5\sigma_n$ sources. The situation is drastically different for the case of the $1''$ resolution image, in which we detected a total of 15 sources with $S_P/\sigma_n \geq 5$ confidence, and all but one is reliably matched to an optical counterpart. The single source that is not reliably matched is $r \approx 0''.65$ from its nearest OIR counterpart. However, this same OIR counterpart (located at a redshift of $z = 2.004$) is reliably matched to a radio counterpart in the $0''.22$ resolution image, and is offset by only $r \approx 0''.093$.

2.4. Using Spectral Indices to Estimate Thermal Fractions

Table 2 lists the radio spectral indices α between 1.4 and 10 GHz of sources found by matching our 10 GHz positions to sources in the 1.4 GHz Morrison et al. (2010) catalog. Their 1.4 GHz images have $1''.7$ resolution and rms noise $\sigma_n \approx 4 \mu\text{Jy beam}^{-1}$. Of the 27 sources detected in the $1''$ -resolution image, we were able to find 1.4 GHz counterparts for 19 of them ($\approx 70\%$). For the 10 GHz sources not having 1.4 GHz counterparts, Table 2 lists lower limits for α , calculated using a 1.4 GHz upper limit of $S_P < 5\sigma_n \approx 19.5 \mu\text{Jy beam}^{-1}$. If we assume all sources have the same non-thermal spectral index, we can use the measured spectral indices to estimate the fractional contributions from thermal emission at the rest-frame frequencies $(\nu_r/\text{GHz}) = 10(1+z)$ for sources having known redshifts z (e.g., Klein et al. 1984; Murphy et al. 2012a). These are given in Table 2, placing limits where necessary. This simple thermal decomposition is sensitive to the estimated

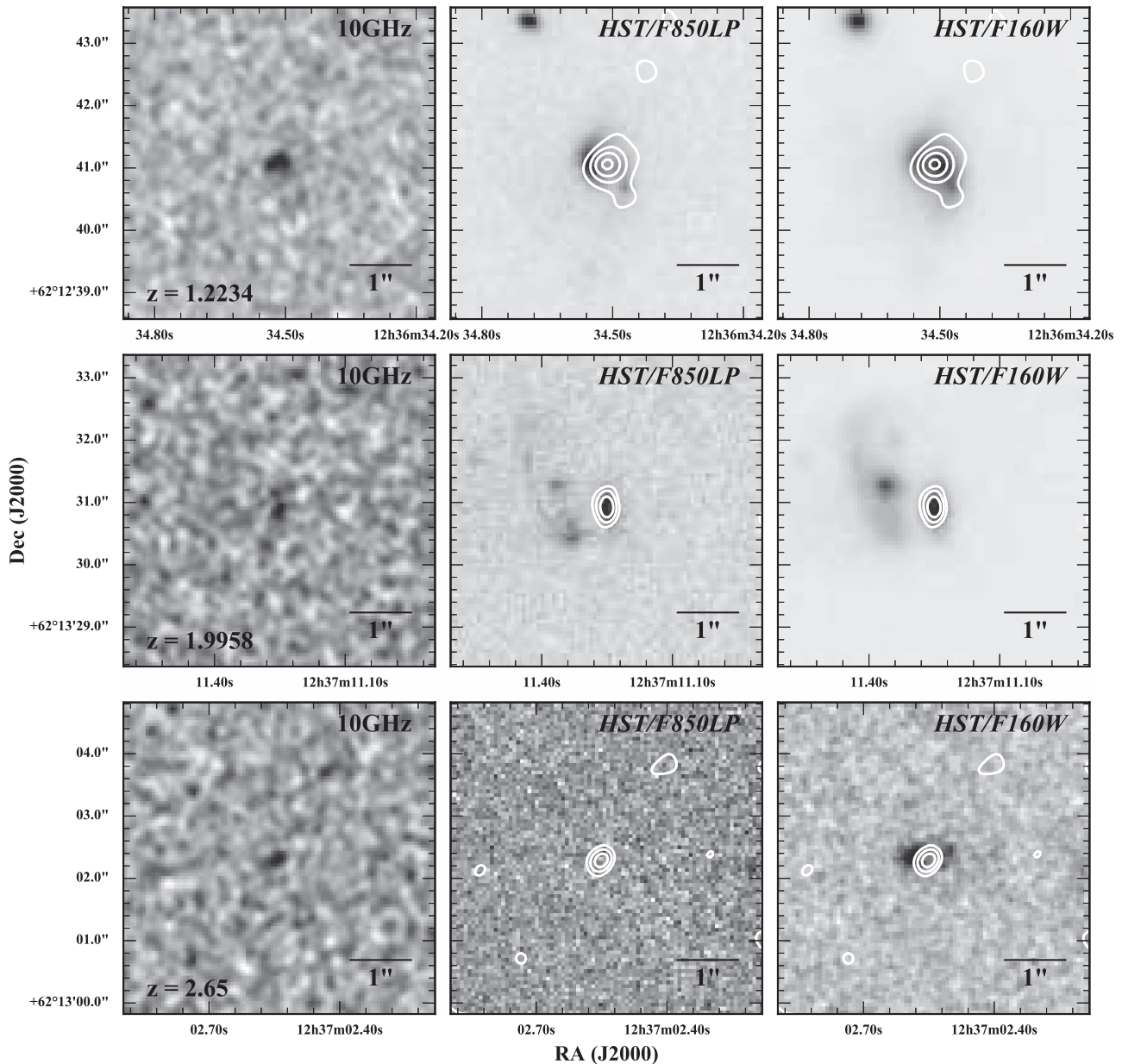


Figure 4. Examples of sources detected in our 10 GHz pilot observations. Also shown are *HST*/ACS z -band and *HST*/WFC3 F160W images, with 10 GHz contours overlaid. Each panel is a $5'' \times 5''$ cutout. Along with redshifts, $1''$ scale bars are shown. The top row illustrates our ability to resolve the two cores in this merging galaxy pair at $z = 1.2234$, whereas the bottom row illustrates our ability to detect optically invisible sources in the radio at high redshifts.

non-thermal spectral index, and assumes that the free-free emission is optically thin at rest-frame frequencies (ν_r/GHz) $\gtrsim 1.4(1+z)$ (e.g., Murphy et al. 2010b), as well as that there is an insignificant contribution of both anomalous microwave emission at ~ 33 GHz (e.g., Murphy et al. 2010a) and thermal dust emission in the rest frequency range $10 \lesssim \nu \lesssim 40$ GHz. We took the non-thermal spectral index to be $\alpha_{\text{NT}} = -0.85$, which is the average non-thermal spectral index found among the 10 star-forming regions studied in NGC 6946 by Murphy et al. (2011b), and very similar to the average value found by Niklas et al. (1997, $\langle \alpha_{\text{NT}} \rangle = -0.83$ with an rms scatter of $\sigma = 0.13$) globally for a sample of 74 nearby galaxies. For those sources having measured spectral indices $\alpha > \alpha_{\text{NT}} = -0.85$, we assigned non-thermal indices $\alpha_{\text{NT}} = \alpha - 0.1$.

3. Results and Discussion

In this section, we present the results for a flux-limited sample of galaxies from this pilot X-band imaging program of GOODS-N, taking advantage of the high angular resolution delivered by the VLA A-configuration, along with its centrally concentrated core of dishes, allowing us to make images with various (u, v) -weightings to improve the brightness temperature sensitivity of the data. As stated in 2.2, the inclusion of the C-configuration data with our imaging helps to fill in the hole in the (u, v) -plane left by the A-configuration data alone. If not accounted for, angular sizes and integrated flux densities of extended sources will be underestimated even in the $1''$ and $2''$ tapered images.

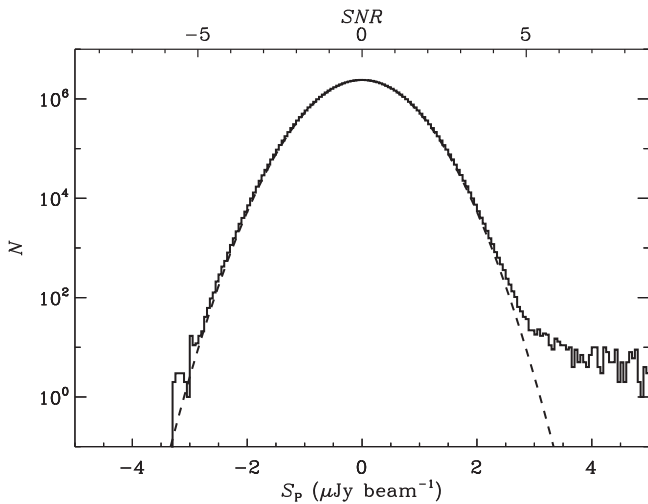


Figure 5. Pixel brightness distribution of the high-resolution image, uncorrected for primary-beam attenuation, over the entire 10 GHz primary beam area used for our source identifications. The bin width is a $0.05 \mu\text{Jy beam}^{-1}$. The dashed line is a Gaussian fit with rms $\sigma = 0.572 \mu\text{Jy beam}^{-1}$ (i.e., the rms measured in the image, out to 5% of the primary beam response). The noise in the 10 GHz image appears Gaussian and is extremely well-behaved.

3.1. Redshift Distributions

The $0''.22$ full-resolution 10 GHz image contains 32 reliable sources at $\geq 3.5\sigma_n$ that have OIR counterparts with measured redshifts. Their median redshift is $\langle z \rangle = 1.24 \pm 0.16$. The $1''$ -resolution image contains 27 sources with OIR counterparts and measured redshifts. The median redshift of these sources is slightly lower, $\langle z \rangle = 1.01 \pm 0.16$, most likely because the $1''$ tapered image is less sensitive to point sources, but more sensitive to the extended sources that will tend to be at lower redshifts. Figure 6 shows the redshift distribution for all 38 unique sources detected in the full-resolution and/or $1''$ tapered images. The median redshift of all sources with OIR counterparts is $\langle z \rangle = 1.24 \pm 0.15$. Figure 6 also shows an excess of sources (7 out of 38) that have redshifts in the narrow range spanning $1.9958 \leq z \leq 2.0180$. These sources are likely members of an over-density traced by sub-mm galaxies (SMGs), optically faint radio sources, and other star-forming galaxies (Chapman et al. 2009). In fact, at least six of the 38 unique 10 GHz-detected sources reported here are $850 \mu\text{m}$ -detected SMGs (Pope et al. 2005; Chapman et al. 2009), four of which appear to be members of this $z \approx 2$ over-density.

3.2. The Size Distribution of $z \sim 1$ Star-forming Disks

Radio astronomers traditionally fit elliptical Gaussians to sources on images and specify source sizes by their deconvolved major and minor FWHM axes θ_M and θ_m . However, the radio brightness distributions of star-forming spiral galaxies are better approximated by optically thin exponential disks, and OIR astronomers often characterize the size of a disk by the effective radius r_e that encloses half of the total flux density of the deprojected disk. Appendix B shows analytically that these two size measures are related by¹⁰

$$\theta_M \approx 2.430 r_e, \quad (11)$$

¹⁰ In this paper, r_e and θ_M are used to describe both linear and angular sizes, with appropriate units labeled.

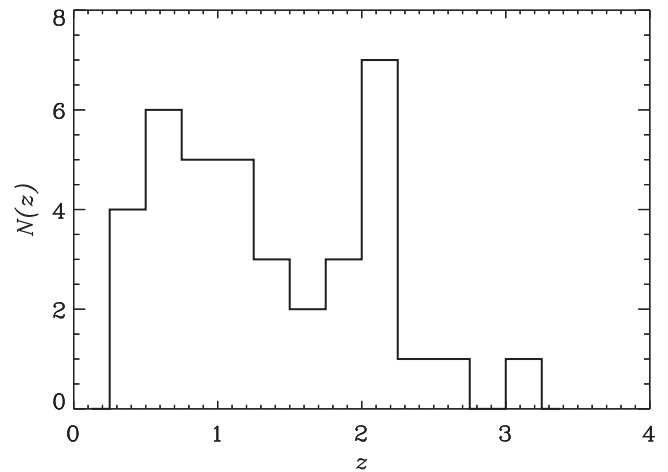


Figure 6. Redshift distribution of all 38 unique sources detected in the full-resolution and/or $1''$ tapered 10 GHz images with $S_p \geq 3.5\sigma_n$ and confirmed by having OIR counterparts. Their median redshift is $\langle z \rangle = 1.24 \pm 0.15$. An excess of sources (7 out of 38) are found in the narrow range of $1.9958 \leq z \leq 2.0180$, and are likely members of an over-density traced by SMGs, optically faint radio sources, and other star-forming galaxies (Chapman et al. 2009).

which we use to compare our radio disk sizes to OIR sizes in the literature.

The major radio-astronomy image analysis packages (e.g., AIPS, CASA) make Gaussian fits, but not exponential ones. These fitting routines are not easily described analytically, so we performed numerical simulations that show Gaussian and exponential fits yield comparable results for both deconvolved sizes and peak brightness-to-integrated flux density ratios S_p/S_I (Appendix C), at least for sources with $r_e \lesssim \theta_{1/2}$.

The distribution of the deconvolved angular sizes for the 32 reliable 10 GHz detections listed in Table 1 is plotted in Figure 7. Among these, the major axes of six sources ($\approx 20\%$) are confidently resolved at $\geq 2\sigma_{\phi_M}$ significance (see Section 2.3), and are identified in Table 1. To determine the typical source size among the entire population of sources, we calculate a weighted median. For each source size, the weight is inversely proportional to the solid angle in which it could have been detected, limited either by S/N or by the area within the 5% primary beam cutoff. The constant of proportionality is set such that a source that could be detected anywhere within the survey area has weight $w_i = 1$, but any constant of proportionality would give the same result. This weight is designed to exactly compensate for the fact that weak extended sources could be seen only in a fraction of the full survey field. Our weighted source size distribution should be representative of a sample that was uniformly selected, unbiased by angular size, over the entire survey area.

The weighted median deconvolved source FWHM is $\langle \theta_M \rangle = 167 \pm 32$ mas, and the weighted rms size scatter is ≈ 91 mas. The corresponding weighted median effective radius is $\langle r_e \rangle = 69 \pm 13$ mas, and the weighted rms scatter in r_e is ≈ 38 mas. Using the measured redshifts of these resolved sources, we plotted their linear sizes as a function of redshift in Figure 8. The weighted median FWHM major axis linear diameter of these sources is $\langle \theta_M \rangle = 1.2 \pm 0.28$ kpc, and θ_M has a weighted rms scatter of ≈ 0.79 kpc. The corresponding weighted median effective linear radius is $\langle r_e \rangle = 509 \pm 114$ pc, and the rms scatter in r_e is ≈ 324 pc. There is no obvious indication of linear size evolution with redshift.

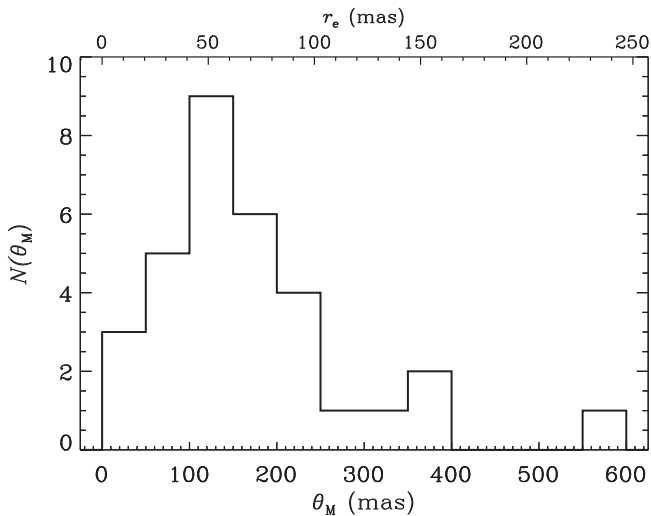


Figure 7. Distribution of deconvolved source FWHM major axes θ_M for all 32 sources detected in the full-resolution image. The corresponding effective radii r_e are marked on the upper abscissa. The weighted median angular size is $\langle\theta_M\rangle = 167 \pm 32$ mas, and the weighted rms scatter in θ_M is 91 mas. The corresponding median effective radius is $\langle r_e\rangle = 69 \pm 13$ mas, and the rms scatter in r_e is 38 mas.

3.2.1. Comparison with Other Radio and mm/sub-mm Sizes

Using a deep VLA 3 GHz image of the Lockman Hole made with $\theta_{1/2} = 0''.66$ resolution, Condon et al. (2017, in preparation) found a preliminary median source size $\theta_M \approx 300 \pm 100$ mas among their detections. Although slightly larger than the 10 GHz sizes reported here, they are actually quite consistent because we expect the 3 GHz radio size to be slightly larger than at 10 GHz, for two reasons: (1) the lower-energy relativistic electrons emitting at 3 GHz may diffuse farther because they have longer synchrotron lifetimes. For rigidity-dependent diffusion of cosmic-rays (CRs), where the magnetic rigidity¹¹ scales as $R^{0.75}$, as measured for CR electrons and protons around 30 Dor (Murphy et al. 2012b), 3 GHz emitting CR electrons will diffuse $\approx 25\%$ further than 10 GHz emitting CR electrons. (2) Thermal emission confined to the star-forming regions contributes a smaller fraction of the total flux density at 3 GHz.

However, the measured radio sizes of our 10 GHz-selected sources are significantly smaller than the 3 GHz sizes reported by Miettinen et al. (2017) for a sample of 115 known SMGs in the COSMOS field. Using sensitive ($\sigma_n \approx 2.4 \mu\text{Jy beam}^{-1}$) 3 GHz images from the VLA-COSMOS 3 GHz Large Project (Smolčić et al. 2017, in press), they found a median source size $\theta_M \approx 590$ mas and an rms size scatter of 420 mas. Given the redshifts of their sources, their median angular size corresponds to a median linear size ≈ 4.5 kpc. That is also close to the median 1.4 GHz size for a sample of 12 SMGs, reported by Biggs & Ivison (2008, i.e., 640 ± 100 mas), which corresponds to a linear size of 5 kpc, given the redshifts of their sources. In contrast, our measured sizes are in much better agreement with the ALMA sizes from Ikarashi et al. (2015) and Simpson et al. (2015), who report median sizes of 200 ± 50 mas (1.6 ± 0.14 kpc) at 1.1 mm, and 300 ± 40 mas (2.4 ± 0.2 kpc)

¹¹ Magnetic rigidity R is defined as $R = pc/(Ze)$, where p is momentum, c is the speed of light, and Ze is the particle charge. Thus, for protons and electrons, $R = \sqrt{E_{\text{CR}}^2 - E_0^2}$, where E_{CR} is the CR energy and E_0 is the particle rest-mass energy.

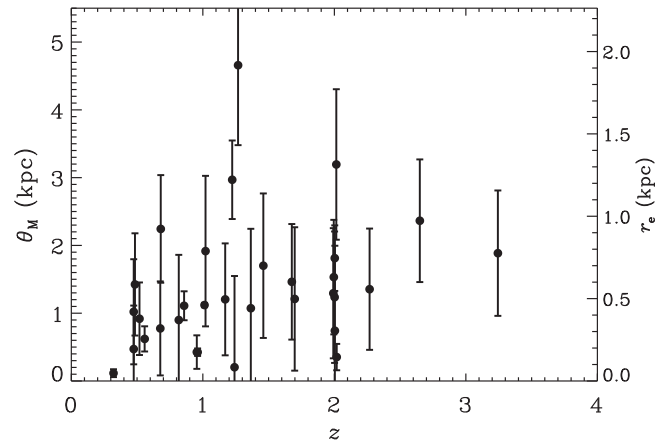


Figure 8. FWHM major-axis linear sizes of all 32 detected sources, plotted against redshift. The corresponding effective radii (r_e) are marked along the right ordinate. The FWHM linear sizes have a weighted median 1.3 ± 0.28 kpc and a weighted rms scatter ≈ 0.79 kpc. The corresponding effective radii r_e have a weighted median 509 ± 114 pc and a weighted rms scatter ≈ 324 pc. No obvious evolution in 10 GHz radio size is seen with redshift.

at $870 \mu\text{m}$, respectively. Thus, although our radio sizes are not for a sample of SMGs, which may be different from the more typical star-forming galaxies selected at 10 GHz, it is interesting to find that our radio sizes are compatible with the high-resolution, dust-emitting sizes of SMGs.

One might expect sub-mm sizes to be different from the radio-emitting sizes, given the different selection criteria. SMGs selected at sub-mm wavelengths may be intrinsically different from star-forming galaxies selected by synchrotron or free-free emission at cm wavelengths because the sub-mm galaxies have no K -correction, and thus are intrinsically more luminous and at higher redshifts than cm-selected galaxies. Furthermore, even for the same galaxy population, the size measured at sub-mm wavelengths may be different (larger) than the size measured at cm wavelengths, because the sub-mm size is that of the cold cirrus dust distribution, whereas the cm size is closer to that of the current star formation.

3.2.2. Comparing Radio, $H\alpha$, and Optical Sizes

We also compared our star-forming galaxy disk sizes to those reported by Nelson et al. (2016), which are based on stacking resolved $H\alpha$ and $H\beta$ emission-line images from the 3D-*HST* survey. By comparing their $H\alpha$ and $H\beta$ galaxy images, these authors could apply an extinction correction to their $H\alpha$ images before fitting for the effective radius. This extinction correction significantly lowers the measured sizes because it multiplies the inferred star-formation rates in the central $r < 1$ kpc of galaxies, with $9.8 < \log(M/M_\odot) < 11.0$, by a factor of ≈ 6 . The average extinction-corrected $H\alpha$ radial profile of these galaxies declines by a factor of ≈ 100 between the center and $r \approx 2$ kpc, which corresponds to an effective radius of $\langle r_e(H\alpha)\rangle \approx 0.73$ kpc. Before making the extinction correction, Nelson et al. (2012) reported a median $H\alpha$ effective radius $\langle r_e\rangle = 4.2 \pm 0.1$ kpc for a sample of 57 strongly star-forming galaxies in the same mass range. Thus, the uncorrected r_e is approximately six times larger than the corrected r_e . The effective radius of the extinction-corrected $H\alpha$ radial profiles is not significantly larger than our weighted median $\langle r_e\rangle \approx 0.51 \pm 0.11$ kpc with rms scatter 0.32 kpc at 10 GHz,

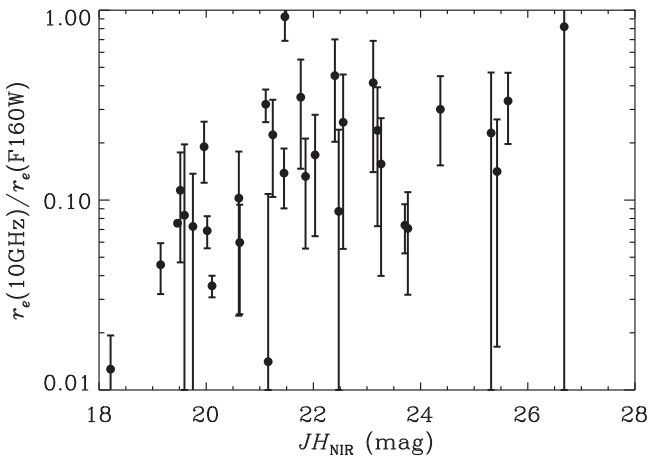


Figure 9. Ratio of 10 GHz-to-*HST*/WFC3 F160W (van der Wel et al. 2014) continuum effective radii, plotted as a function of NIR magnitude for all 32 sources reliably detected in the full-resolution radio image. On average, the 10 GHz sizes are 0.14 ± 0.05 times the rest-frame optical size (not corrected for extinction), and the size ratios have an rms scatter of 0.21, indicating that star formation in our sample of $z \sim 1$ star-forming galaxies is centrally concentrated.

and is much more consistent with the radio sizes reported here than with others in the literature. The small difference between our measured sizes and the extinction-corrected $H\alpha$ sizes might result from underestimating extinctions in the centers of the most massive galaxies in Nelson et al. (2016).

The effect of extinction may also be contributing to what is found in Figure 9, which plots the ratio of the 10 GHz effective radius, as a function of NIR magnitude, to the rest-frame optical continuum r_e reported by van der Wel et al. (2014). The rest-frame optical data used were not corrected for extinction. The star-forming disks measured at 10 GHz, which are similar to the extinction-corrected $H\alpha$ sizes reported by Nelson et al. (2016), are significantly smaller than the uncorrected rest-frame optical continuum sizes. The median 10 GHz-to-F160W size ratio is 0.14 ± 0.05 , and the size ratios have an rms scatter of 0.21. Consequently, star formation appears to be centrally concentrated in this sample of $z \sim 1$ galaxies.

Here, we have converted the deconvolved Gaussian fits to the radio sizes to half-light radii r_e , assuming the conversion for exponential profiles discussed in Appendix B. The *HST*/WFC3 sizes from van der Wel et al. (2014), r_e (F160W), were derived from Sérsic (1963, 1968) profile model fitting, and thus may not exactly match exponential fits (i.e., Sérsic index $n = 1$) on a galaxy-by-galaxy basis. Moreover, the *HST*/WFC3 F160W filter measures optical rest-frame starlight at the mean redshift of our 10 GHz-selected sample, and thus may not perfectly reflect the distribution of optically bright star formation in each galaxy. Nevertheless, it seems clear from Figure 9 that the 10 GHz radio (and $H\alpha$) sizes are uniformly and significantly smaller than the optical galaxy sizes derived from the CANDELS *HST* images that are not corrected for extinction. Accordingly, similar to what has been shown for $H\alpha$ sizes, extinction may be playing a role.

3.2.3. S_p/S_l Ratios of Randomly Oriented Thin Disks

If star-forming galaxies are randomly oriented, transparent, thin, circular exponential disks at radio wavelengths, they should appear elliptical on the sky, with minor axes shortened

by $\theta_m/\theta_M = \cos(i)$, where i is the inclination angle between the disk normal and the line of sight. However, the minor axes θ_m of many galaxies in Table 1 are not resolved, which necessitates another way to check this hypothesis. One way is to use the ratio S_p/S_l of peak brightness to integrated flux density, a quantity that depends on both θ_M and θ_m , and is available for all galaxies. The dependence of S_p/S_l on galaxy size and inclination is derived in Appendix C. The results are shown as functions of r_e in Figure 10. They are consistent with most of our radio sources being randomly oriented, thin, circular exponential disks.

3.3. Spectral Indices and Thermal Fractions

Using the $1''$ and $2''$ resolution images, which bracket the $1''.7$ resolution of the Morrison et al. (2010) 1.4 GHz image, we are able to measure radio spectral indices with nearly matched resolution (see Table 2). Among the 19 sources with 1.4 GHz counterparts, the median observed spectral index between 1.4 and 10 GHz is $\langle \alpha_{1.4}^{10 \text{ GHz}} \rangle \approx -0.74 \pm 0.10$, with a standard deviation of $\sigma_{\alpha_{1.4}^{10 \text{ GHz}}} \approx 0.35$. This median is consistent with what is measured for star-forming galaxies in the local universe (e.g., Condon 1992). However, after including the eight sources (30% of our detections) that have only 1.4 GHz upper limits, the median flattens significantly to $\gtrsim -0.61$. The large number of sources without 1.4 GHz counterparts is not that surprising because, as stated in Section 2.2, the 10 GHz images are ≈ 2 times more sensitive than the 1.4 GHz image of Morrison et al. (2010) for a source with spectral index of -0.7 . Even so, it appears that there is a significant fraction of sources at $z \gtrsim 1$ that have somewhat flat spectral indices, suggesting that higher-frequency radio measurements may indeed be more sensitive to free-free emission, and consequently a more robust measure for the current star formation activity in such systems. Figure 11 plots the measured spectral indices against redshift, for which there is no clear trend.

As discussed in Section 2.4, by assuming a fixed, non-thermal spectral index for each source, we can use the measured spectral indices to estimate the fractional contributions from thermal emission at the rest-frame frequency (ν_r/GHz) = $10(1+z)$ (e.g., Klein et al. 1984; Murphy et al. 2012a), which are listed in Table 2. These estimates additionally assume that the observed 10 GHz emission is powered by star formation. For the 19 sources with 1.4 GHz counterparts, the median redshift corresponds to a rest-frame frequency of ≈ 20 GHz, for which we estimate a median thermal fraction of $26 \pm 0.09\%$ with an rms scatter of 31%. If we additionally include the eight sources for which we only have upper limits at 1.4 GHz, the median redshift also corresponds to a rest-frame frequency of ≈ 20 GHz, and places a lower limit on the median thermal fraction of $\gtrsim 48\%$. Although we have assumed a non-thermal spectral index of -0.85 , one caveat is that spectral steepening in the rest-frame near 20 GHz (e.g., from increased synchrotron and inverse-Compton losses), which is extremely difficult to measure, could result in underestimates of the thermal fractions.

3.3.1. Comparison with Previous Deep X-band Imaging

Our $2''$ tapered image can be compared with the X-band image of Richards et al. (1998). They detected 29 sources stronger than $5\sigma_n$ in a field of radius of $4'.6$ (truncated at $\approx 8\%$ of the primary beam response) in their 8.5 GHz image centered

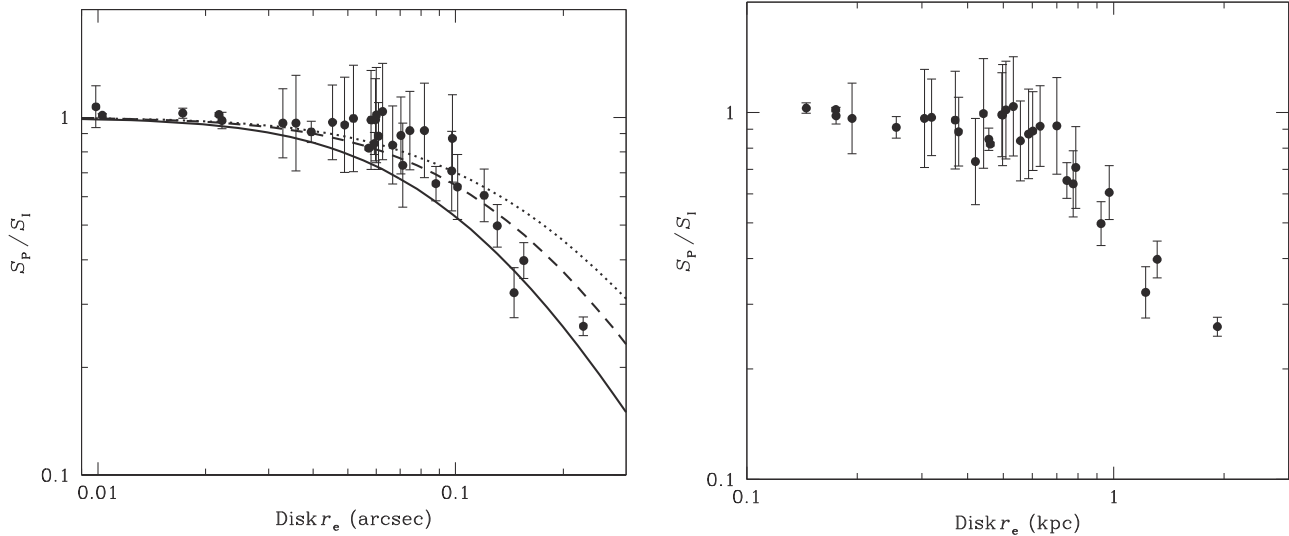


Figure 10. Left: measured ratios S_P/S_I of peak brightness-to-integrated flux densities for all sources detected in our $0''.22$ -resolution image vs. the deconvolved disk effective radius r_e in units of arcsec. The solid curve was calculated from Equation (28) for a circular (face-on) exponential disk. The dashed curve was calculated from Equation (29) for the median inclination angle $i = 60^\circ$ [$\cos(i) = 0.5$] of randomly oriented disks, and the dotted curve corresponds to a nearly edge-on disk with $\cos(i) = 0.25$. The data points should lie between the solid and dotted curves and be centered around the dashed curve. Right: the same as the left panel, except that the abscissa units are in kpc instead of arcsec for sources with measured redshifts.

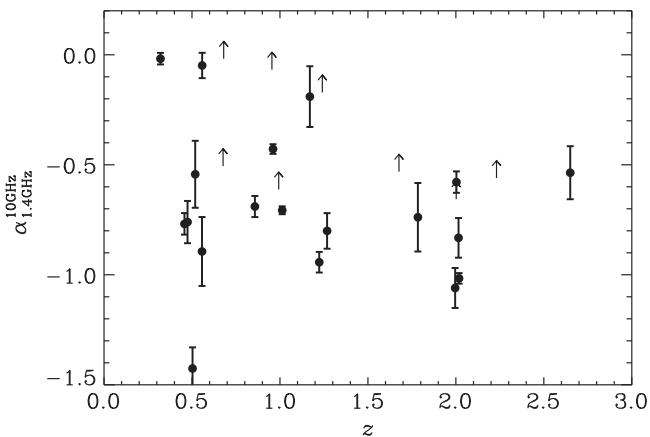


Figure 11. Median spectral index among all 19, 1.4 GHz detected sources is $\langle \alpha_{1.4\text{GHz}}^{10\text{GHz}} \rangle \approx -0.74 \pm 0.10$, with a standard deviation of 0.35. Including the additional eight sources for which there are only upper limits on the 1.4 GHz flux density flattens the median spectral index of our full flux-limited sample selected at 10 GHz to $\langle \alpha_{1.4\text{GHz}}^{10\text{GHz}} \rangle \gtrsim -0.61$.

on the *Hubble* Deep Field. For the original VLA system, the primary beam FWHM at 8.5 GHz is $\approx 5''.2$. Their 8.5 GHz VLA data from the A, BnA, C, DnC, and D configurations respond to sources up to $10''$ in size. The bulk of their observing time was in the C configuration, and their final image had resolution $\theta_{1/2} \approx 3''.5$ and rms noise $\sigma_n \approx 1.8 \mu\text{Jy beam}^{-1}$, corresponding to a brightness-temperature sensitivity $\sigma_n \approx 2.5 \text{ mK}$. This is similar to our $\sigma_n = 1.5 \mu\text{Jy beam}^{-1}$ rms, which scales to $\approx 1.7 \mu\text{Jy beam}^{-1}$ at 8.5 GHz for a source with typical spectral index $\alpha = -0.7$, and a 4.7 mK brightness temperature rms achieved in our $2''$ image.

In our $2''$ resolution image, we detected a total of 14 sources with $S_P/\sigma_n \geq 5$ that are reliable (i.e., the same $5\sigma_n$ sources we consider to be reliable in our $1''$ -resolution image). Given the ratio of primary beam solid angles $\Omega_{10\text{GHz}}/\Omega_{8.5\text{GHz}} = 0.67$ and

sensitivities at the two frequencies, we would expect them to detect $\approx 50\%$ more sources (i.e., ≈ 21 sources). This prediction is slightly more than 1σ smaller than what counting errors would suggest. However, if we were to include the single 5σ detection that is considered unreliable from our $2''$ tapered image, or exclude the four $S_P > 5\sigma_n$ sources in the Richards et al. (1998) sample that were not matched to optical counterparts, our numbers agree to within 1σ of the counting errors.

3.4. A Revised Redshift and Spectral Energy Distribution Analysis for VLA J123642+621331

We detected the radio source VLA J123642+621331 described by Waddington et al. (1999) as a compact [$r_e(\text{F160W}) \approx 0''.2$] star-forming galaxy containing an AGN. The 10 GHz flux density measured in our $1''$ tapered image is consistent with the 8.5 GHz flux density of $\approx 70 \mu\text{Jy}$ reported by Richards et al. (1998, 1999). The source is detected in both our $0''.22$ and $1''$ resolution images, with deconvolved major axes of $42 \pm 23 \text{ mas}$ and $0''.65 \pm 0''.06$, respectively. This suggests a compact core, and is consistent with the upper limit $< 0''.1$ reported by Richards et al. (1998) in their lower signal-to-noise $0''.2$ resolution image. VLA J123642+621331 was resolved by high-resolution ($0''.15$) 1.4 GHz VLA+MERLIN observations (Muxlow et al. 1999), which showed that 10% of the flux density resides in an extended component lying to the east of an unresolved core. The unresolved, compact core was additionally detected by the European VLBI Network (EVN) at 1.6 GHz, providing an upper limit on the core size of 20 mas and corresponding 1.6 GHz brightness temperature of $T_b > 2 \times 10^5 \text{ K}$ (Garrett et al. 2001), indicating that the core emission is dominated by an AGN (Condon et al. 1991).

Waddington et al. (1999) reported a redshift $z = 4.424$ for this source, on the basis of a single emission line detected with Keck/LRIS at 6595 \AA , interpreted to be Lyman α , which is apparently offset by about $1''$ from the optical galaxy position. However, more recent multiwavelength photometric data in the GOODS-N field suggest that the galaxy may instead have a

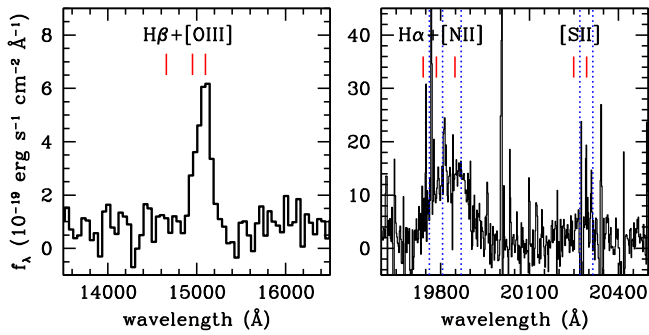


Figure 12. Left: a portion of the *HST*/WFC3 G140 grism spectrum of VLA J123642+621331, showing the emission feature identified as the [O III] doublet. Right: a portion of the Keck/MOSFIRE spectrum. The red tickmarks indicate the predicted wavelengths of the [N II] and H α emission lines, based on the redshift fit to the WFC3 grism spectrum ($z_{[\text{O III}]}$ = 2.015). The broad, blended H α + [N II] complex seems to be redshifted slightly with respect to these predictions, with a visual estimate ($z = 2.018 \pm 0.003$) indicated by the dashed blue lines.

lower redshift, due to faint but significant detection in the GOODS *HST*/ACS *B*-band (F435W) image, as well as mid- to far-infrared photometry (and sub-mm upper limits) that seem inconsistent with $z = 4.4$. A slitless spectrum from the *HST*/WFC3 G140 grism (GO-11600, PI Benjamin Weiner) detects a strong, slightly asymmetric line (Figure 12, left), which we interpret as the blended [O III] 4959,5007 Å doublet, with no detectable H β [$f(5007)/f(\text{H}\beta) > 4.6$ at 2σ]. A constrained two-Gaussian fit to the extracted grism spectrum yields a redshift $z_{[\text{O III}]} = 2.015$.

We then obtained a *K*-band spectrum of VLA J123642+621331 with MOSFIRE on the Keck 1 telescope on UT 2014 April 13, under photometric conditions, using a slit width of 0".7, for a total exposure time of 84 minutes. The data were reduced using the standard MOSFIRE data reduction pipeline (version 2014.06.10). Figure 12 (right) shows a 2"-wide extraction for a portion of the spectrum. A broad (≈ 175 Å) feature is detected, centered at approximately 19825 Å. We interpret this as a blend of broad H α plus [N II]. The complex appears to be slightly offset from the wavelengths predicted based on the fit to [O III] in the grism data. We cannot formally fit the lines, but we estimate $z = 2.018$ from the MOSFIRE spectrum.

This redshift difference with respect to that from [O III] ($\Delta z = 0.003$) is easily consistent with typical uncertainties in *HST*/WFC3 grism spectral measurements (Momcheva et al. 2016). The 6595 Å line reported by Waddington et al. (1999) would not correspond to any emission features commonly seen in distant galaxies or AGN, and it may be a serendipitous detection of another faint, nearby galaxy at a different redshift (perhaps indeed Lyman α), or it could be spurious. The apparently broad H α emission, high [O III]/H β ratio, and perhaps strong [N II] all suggest that an AGN dominates the optical rest-frame nebular line emission. This IR-luminous, radio-loud AGN could be another member of an over-dense structure at $\langle z \rangle = 1.99$ traced by sub-mm-, radio-, and UV-selected star-forming galaxies (Chapman et al. 2009).

The WFC3 grism spectrum of J123642+621331 was also analyzed by Ciardullo et al. (2014), who derived $z = 2.018$, and in the 3D-*HST* catalog of Momcheva et al. (2016), who derived $z = 2.012 \pm 0.002$ (68% confidence).

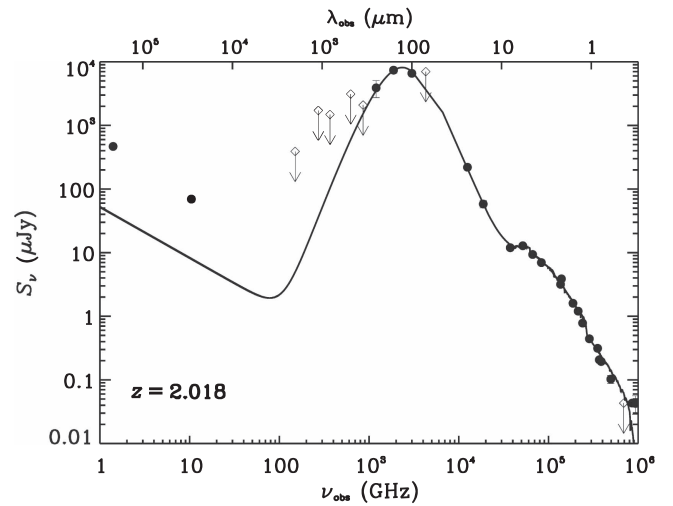


Figure 13. Best-fit radio-to-optical spectral energy distribution of VLA J123642+621331. Data used in the fitting was taken from the literature: OIR data—CANDLES GOODS-N multiwavelength catalog (G. Barro et al. 2016, in preparation); *Spitzer* and *Herschel* far-infrared data (Magnelli et al. 2011; Teplitz et al. 2011; H. Inami et al. 2016, in preparation); SCUBA sub-mm data (Borys et al. 2003; Pope et al. 2005); 1.16 mm AzTEC +MAMBO data (Penner et al. 2011); 2 mm GISMO data (Staguhn et al. 2014). The radio data were not used to constrain the fit, which assumes the standard far-infrared–radio correlation and a typical radio spectrum with $S_\nu \propto \nu^{-0.8}$. The best-fit spectral energy distribution is characterized by a stellar mass of $M_* = 2.4 \times 10^{10} M_\odot$, a stellar mass fraction of $f_* = 0.4$, an infrared (IR; 8–1000 μm) luminosity of $L_{\text{IR}} = 2.3 \times 10^{12} L_\odot$, and a dust temperature of $T_{\text{dust}} = 70$ K, which is extremely hot even when compared to local AGN (e.g., Spinoglio et al. 1995; Andreani et al. 2002). The measured logarithmic far-infrared–radio ratio of $q = 1.19$ has a factor of ≈ 30 times (i.e., 5.6σ) more radio emission compared to the locally measured value for star-forming galaxies, also indicating the presence of an AGN.

Using a compilation of radio-to-optical data in the literature, we fit the full spectral energy distribution of VLA J123642+621331, which is shown in Figure 13. The radio data were not used to constrain the fit, which assumes the standard far-infrared–radio correlation and a typical radio spectrum with $S_\nu \propto \nu^{-0.8}$. The OIR data were fit with the updated Bruzual & Charlot (2003) stellar templates that have an exponentially declining star formation history, with a characteristic timescale of $\tau = 0.1$ Gyr. They are extinguished by an $A_V = 2.4$, assuming a local starburst attenuation law (Calzetti et al. 2000). The mid-infrared emission powered by hot dust was fit by a power law, whereas the far-infrared is fit by a cold dust model (i.e., a modified black body with $\beta_{\text{dust}} = 1.9$). The best-fit spectral energy distribution is characterized by a stellar mass of $M_* = 2.4 \times 10^{10} M_\odot$, a stellar mass fraction of $f_* = 0.4$, an IR luminosity of $L_{\text{IR}} = 2.3 \times 10^{12} L_\odot$, and a dust temperature of $T_{\text{dust}} = 70$ K.

Taking the observed 1.4 GHz flux density of 494.2 μJy (Morrison et al. 2010) and the measured 1.4-to-10 GHz spectral index of -1.02 in Table 2, the corresponding *K*-corrected logarithmic IR–radio ratio is $q_{\text{IR}} = 1.19$, which exhibits a factor of ≈ 30 (i.e., 5.6σ) radio excess compared to the locally measured value of 2.64 (Bell 2003), and thus strongly suggests the presence of an AGN. The far-infrared emission peak at 30 μm in the rest frame implies a remarkably high dust temperature, similar to that seen in a minority of 3C sources (e.g., Spinoglio et al. 1995; Andreani et al. 2002). This fact suggests that the AGN dominates the bolometric luminosity of this source.

We have presented exquisite multiwavelength data on a radio galaxy at $z = 2.018$. The change in redshift for this source from the previously claimed $z = 4.424$ highlights the dangers in single-line redshift determination, especially when the ancillary photometry is poor; for example, similar criteria have been used to claim the detection of a $z = 4.88$ radio galaxy (Jarvis et al. 2009). With the accurate spectral energy distribution we have of VLA J123642+621331, we can predict the colors of $z > 2$ radio galaxies that will be detected in forthcoming wide-area radio surveys such as the Evolutionary Map of the Universe (EMU; Norris et al. 2011, 1.4 GHz; $5\sigma \approx 50 \mu\text{Jy}$; $\theta_{1/2} \approx 10''$) and VLA Sky Survey (VLASS; Murphy & VLASS Survey Science Group 2015, 3 GHz; $5\sigma \approx 345 \mu\text{Jy}$; $\theta_{1/2} \approx 2''.5$). Sources like VLA J123642+621331 at $z \sim 3$ would have flux densities of $0.45 \mu\text{Jy}$ in the H -band, $0.9 \mu\text{Jy}$ in the K -band, and $S_{1.4 \text{ GHz}}/S_K$ ratios of ≈ 170 . It would therefore be challenging to detect their counterparts in wide-field NIR surveys such as those that will be undertaken with *EUCLID*. At $z \sim 5$, which is the limit at which such a source would be detected in the EMU survey, it would be 60 nJy in the H -band, 130 nJy in the K -band, and $0.5 \mu\text{Jy}$ at $3.6 \mu\text{m}$. These are challenging sensitivities to achieve, partly due to source confusion in the latter case. Confirming the redshifts of such sources will instead benefit from spectroscopy at sub-mm/mm frequencies, because the equivalent $z \sim 5$ source would be $150 \mu\text{Jy}$ and $80 \mu\text{Jy}$ at $850 \mu\text{m}$ and 1.2 mm , respectively, which is achievable with ALMA and NOEMA. In summary, the low stellar mass of VLA J123642Q+621331 suggests that it will be difficult to obtain OIR spectroscopic redshifts of high-redshift ($z > 3$) radio galaxy candidates, and mm spectroscopy of [C II] may be the most compelling approach.

4. Conclusions

In this paper, we have presented results from our pilot VLA 10 GHz survey of GOODS-N, aimed at resolving compact starbursts in the redshift range between $1 \lesssim z \lesssim 3$. This deep, single-pointing image reaches an rms noise $\sigma_n = 572 \text{ nJy beam}^{-1}$ and has $\theta_{1/2} = 0''.22$ resolution. Our conclusions can be summarized as follows:

1. The median redshift among the 38 unique sources detected in the full-resolution and/or $1''$ tapered 10 GHz images confirmed by having OIR counterparts is $\langle z \rangle = 1.24 \pm 0.15$.
2. Of the 32 sources reliably detected at 10 GHz in the image with $0''.22$ FWHM resolution, the weighted median of their deconvolved FWHM major axes is $\langle \theta_M \rangle = 0''.17 \pm 0''.03$, and the weighted rms size scatter is $\approx 0''.09$. The weighted median linear major-axis FWHM size of these sources is $\langle \theta_M \rangle = 1.2 \pm 0.28 \text{ kpc}$, and the weighted rms scatter in the linear sizes is $\approx 0.79 \text{ kpc}$. In units of effective radius r_e , these values are equal to $\langle r_e \rangle = 69 \pm 13 \text{ mas}/508 \pm 114 \text{ pc}$, with corresponding rms scatter $\approx 38 \text{ mas}/324 \text{ pc}$. We found no evidence for evolution in radio size with redshift. Our 10 GHz source sizes are significantly smaller than lower-frequency radio sizes reported in the literature, but they appear to agree with high-resolution mm/sub-mm sizes that trace dust emission and with extinction-corrected $H\alpha$ sizes. This result indicates that star formation near the cosmic star formation rate peak largely occurs in relatively compact regions within galaxies.

3. For the detections in our $1''$ -resolution 10 GHz image that have 1.4 GHz counterparts, we measured a median spectral index $\langle \alpha_{1.4 \text{ GHz}}^{10 \text{ GHz}} \rangle \approx -0.74 \pm 0.10$, and the spectral indices have an rms scatter $\sigma_{\alpha_{1.4 \text{ GHz}}^{10 \text{ GHz}}} \approx 0.35$, consistent with what is measured for star-forming galaxies in the local universe and the measurement errors in α . Adding the sources with only upper limits to their 1.4 GHz flux densities places a lower limit on the median spectral index $\langle \alpha_{1.4 \text{ GHz}}^{10 \text{ GHz}} \rangle \gtrsim -0.61$, indicating that a significant fraction of $z \gtrsim 1$ sources selected at 10 GHz have relatively flat spectra, which may indicate that free-free emission contributes significantly and makes their total flux densities robust measures of the current star-formation activity in such sources.
4. Using the spectral indices measured for detections in the $1''$ -resolution 10 GHz image with 1.4 GHz counterparts, and assuming a typical non-thermal spectral index for each source (i.e., $\alpha_{\text{NT}} \approx -0.85$), we estimate a median thermal fraction of $26 \pm 0.09\%$, with a standard deviation of 31%, for a median rest-frame frequency of $\approx 20 \text{ GHz}$. Additionally including the eight sources that have only upper limits for the 1.4 GHz flux densities places a lower limit on the median thermal fraction of $\gtrsim 48\%$ at the same median rest-frame frequency of $\approx 20 \text{ GHz}$.
5. Using a combination of *HST*/WFC3 G140 grism and MOSFIRE spectroscopy, we measured a new redshift for VLA J123642+621331 of $z = 2.018$ that is significantly lower than the $z = 4.424$ previously reported in the literature. Using data from the radio into the optical, the best-fit spectral energy distribution is characterized by a stellar mass of $M_* = 2.4 \times 10^{10} M_\odot$, a stellar mass fraction of $f_* = 0.4$, an IR luminosity of $L_{\text{IR}} = 2.3 \times 10^{12} L_\odot$, and an extremely hot dust temperature of $T_{\text{dust}} = 70 \text{ K}$.

We would like to thank the anonymous referee for very useful comments that helped to improve the content and presentation of this paper. E.J.M. thanks G. Brammer and P. van Dokkum for useful discussions that helped improve this paper. E.J.M. also thanks K. Nyland for helping with figure preparation, D. Riechers for providing unpublished source positions to help prepare these observations, and A. Pope for providing additional data to help with the analysis. The National Radio Astronomy Observatory is a facility of the National Science Foundation operated under cooperative agreement by Associated Universities, Inc. E.J.M. gratefully acknowledges the hospitality of the Aspen Center for Physics, which is supported by the National Science Foundation Grant No. PHY-1066293.

Appendix A Notes on Specific Redshifts

The source in Table 1 with coordinates $\alpha = 12^{\text{h}}36^{\text{m}}44^{\text{s}}.110$, $\delta = +62^\circ 12' 44''.81$ (also listed in Table 2) has a grism-based redshift of $z = 1.676$ reported by Momcheva et al. (2016), with a 68% confidence interval of 1.631–1.705. A deeper inspection of the 3D-*HST* data products suggest that this redshift estimate is primarily derived from the galaxy photometry, with little contribution from the grism data. The extracted spectrum is truncated, and covers only 6% of the normal grism spectral range. No obvious emission or absorption features are detected. The corresponding photometric redshift provided by

Momcheva et al. (2016) is $z = 1.694$, with a similar 68% confidence interval.

For one source included in Table 1 with coordinates $\alpha = 12^{\text{h}}37^{\text{m}}02^{\text{s}}.539$, $\delta = +62^{\circ}13'02''.32$ (also listed in Table 2), the photometric redshift reported in Momcheva et al. (2016) is $z = 5.04$, which is unusually high compared to the other 10 GHz sources. The galaxy is extremely red (see Figure 4), and surprisingly bright in *Spitzer*/IRAC for such a high redshift. The CANDELS team photometric redshift (G. Barro et al. 2017, in preparation; D. Kodra et al. 2017, in preparation) for this galaxy is $z = 2.65$, with a 95% confidence interval 2.21 to 3.16, which we believe to be more reliable.

In Table 1, the source with coordinates $\alpha = 12^{\text{h}}36^{\text{m}}40^{\text{s}}.306$, $\delta = +62^{\circ}13'31''.14$ is taken to be at $z = 0.484$, based on a Keck/LRIS spectrum (Cohen et al. 2000; Cowie et al. 2004). Barger et al. (2008) report $z = 0.4352$, based on Keck/DEIMOS data, whereas Wirth et al. (2004) observed this galaxy but did not measure a redshift. A. Barger (2017, private communication) reports that the LRIS spectrum is higher in quality, but that the redshift is nevertheless uncertain.

The source in Table 1 with coordinates $\alpha = 12^{\text{h}}36^{\text{m}}57^{\text{s}}.375$, $\delta = +62^{\circ}14'07''.86$ has a tentative (“B-grade”) $z = 1.460$ redshift from unpublished Keck/DEIMOS spectrum (D. Stern et al. 2017, in preparation), based on [O II] 3727 Å emission.

In Table 1, the source with coordinates $\alpha = 12^{\text{h}}36^{\text{m}}46^{\text{s}}.063$, $\delta = +62^{\circ}14'48''.70$ (also listed in Table 2) has a secure (“A-grade”) $z = 2.003$ redshift from unpublished Keck/LRIS spectrum (D. Stern et al. 2017, in preparation), based on detections of Lyman α and C III] 1909 Å. This galaxy was additionally detected by SCUBA at 850 μm (GN12 in Pope et al. 2005).

In Table 2, the source with coordinates $\alpha = 12^{\text{h}}36^{\text{m}}44^{\text{s}}.010$, $\delta = +62^{\circ}14'50''.77$ has a tentative (“B-grade”) redshift of $z = 1.784$ from an unpublished Keck/LRIS spectrum (D. Stern et al. 2017, in preparation), using C IV 1549 Å and Fe II 2600 Å absorption lines. This value is consistent with $z = 1.77$ measured from *Spitzer*/IRS spectroscopy (Kirkpatrick et al. 2012), which shows silicate 9.7 μm absorption indicative of the presence of an obscured AGN. Reddy et al. (2006) also published a redshift of $z = 2.095$ for this source, based on Keck/LRIS spectroscopy. However, it is marked as uncertain in their data table.

Appendix B

Relating Radio and Optical Source Sizes

The point-spread function or “beam” of a telescope is usually a circular Gaussian, and radio astronomers usually describe its resolution in terms of its FWHM beamwidth $\theta_{1/2}$, as defined by:

$$\exp\left[-\frac{(\theta_{1/2}/2)^2}{2\sigma^2}\right] = \frac{1}{2}, \quad (12)$$

where σ is the rms width of the Gaussian and σ^2 is its variance. Thus,

$$\theta_{1/2} = (8 \ln 2)^{1/2} \sigma \approx 2.35482\sigma. \quad (13)$$

The apparent brightness distribution of a source in an image is the convolution of its actual brightness distribution with the beam. If the source is only slightly resolved, the image brightness distribution is nearly Gaussian and an elliptical Gaussian fit to the image brightness distribution can be used to

estimate the major and minor FWHM axes of the actual “deconvolved” source. Variances add under convolution, so the deconvolved FWHM major and minor axes are

$$\theta_{\text{M}}^2 = \phi_{\text{M}}^2 - \theta_{1/2}^2, \quad (14)$$

$$\theta_{\text{m}}^2 = \phi_{\text{m}}^2 - \theta_{1/2}^2, \quad (15)$$

where ϕ_{M} and ϕ_{m} are the image FWHM sizes. Equation (14) and Equation (15), with $\theta_{1/2} = 0''.22$, were used to calculate the values of θ_{M} and θ_{m} listed in Table 1. For a non-Gaussian source brightness distribution, θ_{M} and θ_{m} may not be FWHM sizes; rather, they indicate only the variance of the source brightness distribution: $\sigma_{\text{M}}^2 = \theta_{\text{M}}^2 / (8 \ln 2)$ and $\sigma_{\text{m}}^2 = \theta_{\text{m}}^2 / (8 \ln 2)$.

Most μJy radio sources are powered by star-forming galaxies whose face-on radio brightness distributions are better approximated by a transparent thin circular disk, the normalized brightness of which declines exponentially with some scale length β :

$$B(r) = \frac{1}{2\pi\beta^2} \exp\left(-\frac{r}{\beta}\right). \quad (16)$$

Optical astronomers typically specify the disk size in terms of its effective radius r_{e} , defined as the radius enclosing half of the total flux density.

$$\frac{1}{2} \equiv 2\pi \int_0^{r_{\text{e}}} B(r) r dr. \quad (17)$$

The relation between β and r_{e} can be calculated by inserting Equations (16) into (17) and integrating to get

$$\frac{1}{2} = \left(1 + \frac{r_{\text{e}}}{\beta}\right) \exp\left(-\frac{r_{\text{e}}}{\beta}\right). \quad (18)$$

Solving Equation (18) numerically yields $r_{\text{e}} \approx 1.67835\beta$. As β is the scale length over which the brightness declines by a factor of $e^1 \approx 10^{0.434}$, r_{e} is the scale length over which the brightness declines by a factor of $e^{1.67835} \approx 10^{0.729}$.

The variance $\langle x^2 \rangle$ of a circular exponential disk is

$$\begin{aligned} \langle x^2 \rangle &\equiv \int_0^{\infty} \int_{\psi=0}^{2\pi} x^2 B(r) r d\psi dr \\ &= \int_{r=0}^{\infty} \int_{\psi=0}^{2\pi} [r \cos(\psi)]^2 B(r) r d\psi dr \end{aligned} \quad (19)$$

$$\begin{aligned} \langle x^2 \rangle &= \frac{1}{2\pi\beta^2} \int_{\psi=0}^{2\pi} \cos^2(\psi) d\psi \int_{r=0}^{\infty} r^3 \exp\left(-\frac{r}{\beta}\right) dr \\ &= \frac{1}{2\beta^2} \int_0^{\infty} r^3 \exp\left(-\frac{r}{\beta}\right) dr. \end{aligned} \quad (20)$$

Integrating by parts three times gives

$$\langle x^2 \rangle = 3\beta^2 \approx 1.0650r_{\text{e}}^2. \quad (21)$$

If a transparent thin face-on circular exponential disk is tilted by inclination angle i , it appears as an elliptical exponential disk whose unchanged major axis θ_{M} measures the disk r_{e} , and whose minor axis θ_{m} has been shortened by the factor $\cos(i)$. In the limit $r_{\text{e}} < \theta_{1/2}$, the image of a tilted exponential disk galaxy is a nearly Gaussian ellipse, and the deconvolved disk major

axis is related to the effective radius by

$$\theta_M = (8 \ln 2 \langle x^2 \rangle)^{1/2} \approx 2.430 r_e. \quad (22)$$

Appendix C

The Ratio of S_P/S_I for an Elliptical Exponential Disk Observed with a Circular Gaussian Beam

If a circular Gaussian beam with attenuation power pattern

$$A(r) = \exp\left(-\frac{r^2}{2\sigma^2}\right) \quad (23)$$

is pointed at a circular source with brightness distribution $B(r)$, the attenuated peak brightness on the image is

$$S_a = 2\pi \int_0^\infty A(r)B(r) r dr. \quad (24)$$

Inserting the brightness distribution of a circular exponential disk (Equation (16)) gives the ratio of peak brightness S_P to the integrated flux density S_I :

$$\begin{aligned} \frac{S_P}{S_I} = S_a &= \frac{2\pi}{2\pi\beta^2} \int_0^\infty \exp\left(-\frac{r^2}{2\sigma^2}\right) \exp\left(-\frac{r}{\beta}\right) r dr \\ &= \frac{1}{\beta^2} \int_0^\infty r \exp\left[-\frac{1}{2\sigma^2}\left(r^2 + \frac{2\sigma^2}{\beta}r\right)\right] dr. \end{aligned} \quad (25)$$

This integral can be evaluated in terms of the complementary error function

$$\begin{aligned} \operatorname{erfc}(z) &\equiv 1 - \operatorname{erf}(z) \\ &= \frac{2}{\sqrt{\pi}} \int_z^\infty \exp(-t^2) dt \end{aligned} \quad (26)$$

for

$$z = s^{-1/2} \left(\frac{\sigma}{\beta}\right) \approx 0.50398 \left(\frac{\theta_{1/2}}{r_e}\right). \quad (27)$$

The result is

$$\frac{S_P}{S_I} = 2z^2 [1 - \sqrt{\pi} z \exp(z^2) \operatorname{erfc}(z)]. \quad (28)$$

Equation (28) is exact only for a circular exponential disk. For an elliptical exponential disk, a very good approximation is the geometric mean of the S_P/S_I values calculated for circular disks that match the z values calculated for the major (M) and minor (m) axes of the ellipse:

$$\frac{S_P}{S_I} \approx \left[\left(\frac{S_P}{S_I}\right)_M \left(\frac{S_P}{S_I}\right)_m \right]^{1/2}. \quad (29)$$

References

Andreani, P., Fosbury, R. A. E., van Bemmel, I., & Freudling, W. 2002, *A&A*, 381, 389
 Barger, A. J., Cowie, L. L., & Wang, W.-H. 2008, *ApJ*, 689, 687
 Bell, E. F. 2003, *ApJ*, 586, 794
 Biggs, A. D., & Ivison, R. J. 2008, *MNRAS*, 385, 893
 Borys, C., Chapman, S., Halpern, M., & Scott, D. 2003, *MNRAS*, 344, 385

Bruzual, G., & Charlot, S. 2003, *MNRAS*, 344, 1000
 Calzetti, D., Armus, L., Bohlin, R. C., et al. 2000, *ApJ*, 533, 682
 Chapman, S. C., Blain, A., Ibata, R., et al. 2009, *ApJ*, 691, 560
 Ciardullo, R., Zeimann, G. R., Gronwall, C., et al. 2014, *ApJ*, 796, 64
 Cohen, J. G., Hogg, D. W., Blandford, R., et al. 2000, *ApJ*, 538, 29
 Condon, J. 2015, arXiv:1502.05616
 Condon, J. J. 1984, *ApJ*, 287, 461
 Condon, J. J. 1992, *ARA&A*, 30, 575
 Condon, J. J. 1997, *PASP*, 109, 166
 Condon, J. J., Balonek, T. J., & Jauncey, D. L. 1975, *AJ*, 80, 887
 Condon, J. J., Huang, Z.-P., Yin, Q. F., & Thuan, T. X. 1991, *ApJ*, 378, 65
 Conway, J. E., Cornwell, T. J., & Wilkinson, P. N. 1990, *MNRAS*, 246, 490
 Cornwell, T. J. 2008, *ISTSP*, 2, 793
 Cornwell, T. J., Golap, K., & Bhatnagar, S. 2005, in ASP Conf. Ser. 347, *Astronomical Data Analysis Software and Systems XIV*, ed. P. Shopbell, M. Britton, & R. Ebert (San Francisco, CA: ASP), 86
 Cornwell, T. J., Golap, K., & Bhatnagar, S. 2008, *ISTSP*, 2, 647
 Cowie, L. L., Barger, A. J., Hu, E. M., Capak, P., & Songaila, A. 2004, *AJ*, 127, 3137
 de Jong, T., Klein, U., Wielebinski, R., & Wunderlich, E. 1985, *A&A*, 147, L6
 Dickinson, M., Giavalisco, M., & GOODS Team 2003, in ESO Astrophysics Symp., *The Mass of Galaxies at Low and High Redshift*, ed. R. Bender & A. Renzini (Garching: ESO), 324
 Elbaz, D., Dickinson, M., Hwang, H. S., et al. 2011, *A&A*, 533, A119
 Frayer, D. T., Koda, J., Pope, A., et al. 2008, *ApJL*, 680, L21
 Garrett, M. A., Muxlow, T. W. B., Garrington, S. T., et al. 2001, *A&A*, 366, L5
 Giavalisco, M., Ferguson, H. C., Koekemoer, A. M., et al. 2004, *ApJL*, 600, L93
 Grogin, N. A., Kocevski, D. D., Faber, S. M., et al. 2011, *ApJS*, 197, 35
 Helou, G., Soifer, B. T., & Rowan-Robinson, M. 1985, *ApJL*, 298, L7
 Hodge, J. A., Riechers, D., Decarli, R., et al. 2015, *ApJL*, 798, L18
 Ikarashi, S., Ivison, R. J., Caputi, K. I., et al. 2015, *ApJ*, 810, 133
 Jarvis, M. J., Teimourian, H., Simpson, C., et al. 2009, *MNRAS*, 398, L83
 Karim, A., Schinnerer, E., Martínez-Sansigre, A., et al. 2011, *ApJ*, 730, 61
 Kirkpatrick, A., Pope, A., Alexander, D. M., et al. 2012, *ApJ*, 759, 139
 Klein, U., & Graeve, R. 1986, *A&A*, 161, 155
 Klein, U., Wielebinski, R., & Beck, R. 1984, *A&A*, 135, 213
 Kobulnicky, H. A., & Johnson, K. E. 1999, *ApJ*, 527, 154
 Koekemoer, A. M., Faber, S. M., Ferguson, H. C., et al. 2011, *ApJS*, 197, 36
 Kroupa, P. 2001, *MNRAS*, 322, 231
 Magnelli, B., Elbaz, D., Chary, R. R., et al. 2011, *A&A*, 528, A35
 Magnelli, B., Popesso, P., Berta, S., et al. 2013, *A&A*, 553, A132
 McMullin, J. P., Waters, B., Schiebel, D., Young, W., & Golap, K. 2007, in ASP Conf. Ser. 376, *Astronomical Data Analysis Software and Systems XVI*, ed. R. A. Shaw, F. Hill, & D. J. Bell (San Francisco, CA: ASP), 127
 Mezger, P. G., & Henderson, A. P. 1967, *ApJ*, 147, 471
 Miettinen, O., Delvecchio, I., Smolčić, V., et al. 2017, arXiv:1702.07527
 Mohan, N., & Rafferty, D. 2015, *PyBDSM: Python Blob Detection and Source Measurement*, Astrophysics Source Code Library, ascl:1502.007
 Momcheva, I. G., Brammer, G. B., van Dokkum, P. G., et al. 2016, *ApJS*, 225, 27
 Morrison, G. E., Owen, F. N., Dickinson, M., Ivison, R. J., & Ibar, E. 2010, *ApJS*, 188, 178
 Murphy, E., Sargent, M., Beswick, R., et al. 2015a, *PoS AASKA14*, 85
 Murphy, E. J. 2009, *ApJ*, 706, 482
 Murphy, E. J., Bremseth, J., Mason, B. S., et al. 2012a, *ApJ*, 761, 97
 Murphy, E. J., Chary, R.-R., Dickinson, M., et al. 2011a, *ApJ*, 732, 126
 Murphy, E. J., Condon, J. J., Schinnerer, E., et al. 2011b, *ApJ*, 737, 67
 Murphy, E. J., Dong, D., Leroy, A. K., et al. 2015b, *ApJ*, 813, 118
 Murphy, E. J., Helou, G., Condon, J. J., et al. 2010a, *ApJL*, 709, L108
 Murphy, E. J., Porter, T. A., Moskalenko, I. V., Helou, G., & Strong, A. W. 2012b, *ApJ*, 750, 126
 Murphy, E. & VLASS Survey Science Group 2015, *PoS EXTRA-RADSUR2015*, 6
 Murphy, T., Cohen, M., Ekers, R. D., et al. 2010b, *MNRAS*, 405, 1560
 Muxlow, T. W. B., Wilkinson, P. N., Richards, A. M. S., et al. 1999, *NewAR*, 43, 623
 Nelson, E. J., van Dokkum, P. G., Brammer, G., et al. 2012, *ApJL*, 747, L28
 Nelson, E. J., van Dokkum, P. G., Momcheva, I. G., et al. 2016, *ApJL*, 817, L9
 Niklas, S., Klein, U., & Wielebinski, R. 1997, *A&A*, 322, 19
 Nikolic, B., & Bolton, R. C. 2012, *MNRAS*, 425, 1257
 Norris, R. P., Hopkins, A. M., Afonso, J., et al. 2011, *PASA*, 28, 215
 Penner, K., Pope, A., Chapin, E. L., et al. 2011, *MNRAS*, 410, 2749

- Perley, R. 2016, Jansky Very Large Array Primary Beam Characteristics, EVLA Memo, 195
- Pope, A., Borys, C., Scott, D., et al. 2005, *MNRAS*, **358**, 149
- Rau, U., & Cornwell, T. J. 2011, *A&A*, **532**, A71
- Reddy, N. A., Steidel, C. C., Erb, D. K., Shapley, A. E., & Pettini, M. 2006, *ApJ*, **653**, 1004
- Richards, E. A., Fomalont, E. B., Kellermann, K. I., et al. 1999, *ApJL*, **526**, L73
- Richards, E. A., Kellermann, K. I., Fomalont, E. B., Windhorst, R. A., & Partridge, R. B. 1998, *AJ*, **116**, 1039
- Sault, R. J., & Wieringa, M. H. 1994, *A&AS*, **108**, 585
- Schinnerer, E., Smolčić, V., Carilli, C. L., et al. 2007, *ApJS*, **172**, 46
- Sérsic, J. L. 1963, *BAAA*, **6**, 41
- Sérsic, J. L. 1968, Atlas de Galaxias Australes (Córdoba: Observatorio Astronomico, Universidad Nacional de Córdoba)
- Simpson, J. M., Smail, I., Swinbank, A. M., et al. 2015, *ApJ*, **799**, 81
- Smolčić, V., Novak, M., Bondi, M., et al. 2017, *A&A*, in press
- Spinoglio, L., Malkan, M. A., Rush, B., Carrasco, L., & Recillas-Cruz, E. 1995, *ApJ*, **453**, 616
- Staguhn, J. G., Kovács, A., Arendt, R. G., et al. 2014, *ApJ*, **790**, 77
- Swinbank, A. M., Smail, I., Chapman, S. C., et al. 2004, *ApJ*, **617**, 64
- Teplitz, H. I., Chary, R., Elbaz, D., et al. 2011, *AJ*, **141**, 1
- Treu, T., Ellis, R. S., Liao, T. X., et al. 2005, *ApJ*, **633**, 174
- Turner, J. L., & Ho, P. T. P. 1983, *ApJL*, **268**, L79
- Turner, J. L., & Ho, P. T. P. 1985, *ApJL*, **299**, L77
- van der Wel, A., Franx, M., van Dokkum, P. G., et al. 2014, *ApJ*, **788**, 28
- Waddington, I., Windhorst, R. A., Cohen, S. H., et al. 1999, *ApJL*, **526**, L77
- Williams, R. E., Blacker, B., Dickinson, M., et al. 1996, *AJ*, **112**, 1335
- Wilman, R. J., Miller, L., Jarvis, M. J., et al. 2008, *MNRAS*, **388**, 1335
- Wirth, G. D., Willmer, C. N. A., Amico, P., et al. 2004, *AJ*, **127**, 3121
- Yun, M. S., Reddy, N. A., & Condon, J. J. 2001, *ApJ*, **554**, 803